JOURNAL OF PETROLOGY | VOLUME 00 | NUMBER 0 | PAGES 1–27 | 2009 | doi:10.1093/petrology/egp024
Journal of Petrology Advance Access published May 11, 2009

Continental Flood Basalts and Mantle Plumes: a Case Study of the Northern Ethiopian Plateau

LUIGI BECCALUVA[1]*, GIANLUCA BIANCHINI[1,2], CLAUDIO NATALI[1] AND FRANCA SIENA[1]

[1]DIPARTIMENTO DI SCIENZE DELLA TERRA, UNIVERSITÀ DI FERRARA, VIA SARAGAT 1, 44100 FERRARA, ITALY
[2]SCHOOL OF GEOLOGY, GEOGRAPHY AND THE ENVIRONMENT, KINGSTON UNIVERSITY, PENRHYN ROAD, KINGSTON UPON THAMES KT1 2EE, UK

RECEIVED MAY 30, 2008; ACCEPTED APRIL 1, 2009

New geochemical data integrated in a petrogenetic model indicate that the ~30 Ma Northern Ethiopian continental flood basalts (CFBs) preserve a record of magmas generated from the centre to the flanks of a plume head, currently corresponding to the 'Afar hotspot'. Basaltic lavas appear zonally arranged with Low-Ti tholeiites (LT) in the west, High-Ti tholeiites (HT1) to the east and very High-Ti transitional basalts and picrites (HT2, TiO_2 4–6 wt %) closer to the Afar triple junction. Modelling provides estimates of the P–T–X *conditions of magma generation showing that the Ethiopian CFBs could be generated in the pressure range 1·3–3·0 GPa at an approximate depth of 40–100 km from mantle sources that were increasingly metasomatized and hotter (1200–1500°C) from west to east; that is, from the outer zones (LT) to the core of the plume head (HT2 ultra-titaniferous basalts and picrites). Metasomatizing agents can be envisaged as alkali–silicate melts that integrate various geochemical components (e.g. Ti and related high field strength elements, low field strength elements, light rare earth elements, H_2O, noble gases, etc.) scavenged and pooled along the plume axis, and derived from heterogeneous mantle materials mixed during the plume rise. This has significant implications for the current debate about mantle plumes, as the modelled compositionally and thermally zoned plume head (*Texcess $\geq$ 300°C *with respect to ambient mantle) is in accordance with seismic tomography and buoyancy flux, as well as geochemical characteristics, thus supporting a deep provenance of the Afar plume, which possibly originated in the transition zone or lower mantle.*

KEY WORDS: *Ethiopian plateau; Afar triangle; continental flood basalts; picrite; mantle plume; petrogenesis; metasomatism; mantle components*

INTRODUCTION

After the pioneering work of Morgan (1971) a renewed interest in mantle plumes has arisen in the last decade, with many controversial hypotheses on the depth of plume provenance, triggering mechanisms, shape and size as well as relationships with hotspots, large igneous provinces (LIPs), and rift volcanism (Ernst & Buchan, 2001; Foulger *et al.*, 2005; Beccaluva *et al.*, 2007*b*; Foulger & Jurdy, 2007).

For continental flood basalt (CFB) provinces such as the Parana–Etendeka, Karoo–Ferrar and Deccan (Hawkesworth *et al.*, 1986, 1988; Macdougall, 1988; Piccirillo & Melfi, 1988; Melluso *et al.*, 1995; Peate, 1997) a relationship with mantle plumes has been widely hypothesized, with the debate gradually focusing on the compositional features of their constituent lavas (High-Ti vs Low-Ti basalts) and their mantle sources, which could include both lithospheric and asthenospheric geochemical components (Ellam & Cox, 1991; Sweeney *et al.*, 1991; Ellam *et al.*, 1992; Gallagher & Hawkesworth, 1992). However, the petrological and physical-chemical characteristics of the mantle sources from which High-Ti and Low-Ti CFBs were generated are still debated and reliable estimates of pressure (P) and temperature (T) of melting are scarce (Farmer, 2003, and references therein).

The East African rift system is of particular interest as large amounts of plateau basalts were erupted during the Tertiary associated with regional uplift (Ethiopian and Kenyan domes), attributed to either one or two distinct mantle plumes (Ebinger & Sleep, 1998; Rogers *et al.*, 2000;

*Corresponding author. E-mail: bcc@unife.it

Yirgu *et al.*, 2006). The Early Oligocene Northern Ethiopia–Yemen volcanic province provides an important natural laboratory as it comprises the entire range of CFB magmas—from Low-Ti to High-Ti and very High-Ti basalts and picrites—erupted in a well-defined space–time interval, and overlain by younger alkaline basalts with peridotite xenoliths, which provide direct evidence of the nature of the mantle section beneath the plateau. Moreover, this CFB province corresponds to the region where Afro-Arabia continental break-up took place with the formation of the Red Sea–Gulf of Aden–East African rift system centred in the Afar 'triple junction', where the possible existence of a deep mantle plume has been suggested mainly on the basis of geophysical data (Hofmann *et al.*, 1997; Davaille *et al.*, 2005).

In this study we present new field and geochemical data integrated in a comprehensive petrogenetic model for the Northern Ethiopian CFBs and mantle xenoliths from the same area, to define for the first time the P–T–X conditions, shape and size of the mantle melting region as well as their bearing on the Afar hotspot. This petrological approach tests the Afar plume hypothesis, integrating the geophysical data with analogue and numerical modelling, and supports the mantle plume theory.

VOLCANO-TECTONIC SETTING

The Northern Ethiopian plateau (Fig. 1) mainly consists of tholeiitic to transitional basaltic lavas (Mohr & Zanettin, 1988), which were erupted at ~30 Ma in a period of 1 Myr or less (Hofmann *et al.*, 1997). The basalts cover an area of ~210 000 km^2 with a lava pile up to 2000 m thick in the central–eastern part, thinning to less than 500 m toward the northern and southern boundaries. On the eastern margin, neighbouring the Afar escarpment, rhyolitic volcanic rocks characterizing the upper part of the sequence have been interpreted as the differentiated products of basaltic magmas that mark the start of continental rifting (Ayalew *et al.*, 2006). Similar nearly coeval CFB volcanism is recorded in the Yemen conjugate margin covering an area of ~80 000 km^2 (Baker *et al.*, 1996; Ukstins *et al.*, 2002). The plateau volcanism in Northern Ethiopia was preceded by uplift (at least since the Late Eocene, based on stratigraphical data: Bosellini *et al.*, 1987) of the underlying basement by up to 1·2 km (Şengör, 2001). After the CFB emplacement, the area was affected by a further ~2 km uplift, as a result of isostatic and tectonic processes (Gani *et al.*, 2007). Dyke swarms, that most probably fed CFB fissure eruptions (Mège & Korme, 2004; Fig. 1), are subparallel to sea-floor spreading axes in the Gulf of Aden and Red Sea, suggesting multiple rifting and spreading processes radiating from the still active Afar zone (e.g. volcano-seismic crisis of autumn 2005; Ayele *et al.*, 2007).

Geographical information system (GIS)-based digitization of the 1:2 000 000 geological map of the region (Merla *et al.*, 1973), carried out as part of this study, permitted the original volume of the flood basalts in the Northern Ethiopian Plateau to be estimated as 250 000 km^3, implying an eruption rate of the order of 0·2–0·3 km^3/year, which is comparable with that of other CFB provinces (Farmer, 2003). The plateau basalts are overlain by huge shield volcanoes mainly composed of alkaline lavas (Mt. Choke and Gugugftu, 22 Ma; Mt. Guna, 10·7 Ma; Kieffer *et al.*, 2004). In the southwestern part of the plateau highly alkaline lavas were erupted from a number of Quaternary volcanic centres. Basanite lavas from two of these volcanoes near Injibara and west of Nekemte (Dedessa River) carry abundant mantle xenoliths, which have also been considered in this study.

New detailed sampling of selected plateau sections has been carried out in four areas (Fig. 2), as follows.

(1) Simien Mountains section (north of Gondar), made up of ~1950 m of basaltic lavas overlying the Mesozoic sedimentary basement.
(2) Adigrat section (west of Adigrat), consisting of ~500 m of basaltic lavas overlying the Precambrian crystalline basement.
(3) Blue Nile section (near Dejen), consisting of ~450 m of basaltic lavas overlying the Mesozoic sedimentary basement.
(4) Lalibela section, made up of ~1800 m of basaltic and picritic lavas (with some rhyolitic intercalations at the top) overlying the Mesozoic sedimentary basement.

ANALYTICAL METHODS

Rock samples were selected from fresh chips and powdered in an agate mill. Major and trace elements (Ni, Co, Cr, V, Sc, Rb, Sr, Zr) were analyzed by X-ray fluorescence (XRF) on powder pellets, using a wavelength-dispersive automated ARL Advant'X spectrometer at the Department of Earth Sciences, Ferrara University. Accuracy and precision for major elements are estimated as better than 3% for Si, Ti, Fe, Ca and K, and 7% for Mg, Al, Mn, Na; for trace elements (above 10 ppm) they are better than 10%. Rare earth elements (REE), Y, Hf, Nb, Ta, Th, and U were analyzed by inductively coupled mass spectrometry (ICP-MS) at the Department of Earth Sciences, Ferrara University, using a VG Plasma Quad2 plus. Accuracy and precision, based on replicated analyses of samples and standards, are estimated as better than 10% for all elements well above the detection limit.

Mineral compositions were obtained at the School of Geography, Geology and the Environment of Kingston University with a Zeiss EVO 50 scanning electron microscope in conjunction with an Oxford Instruments INCA microanalysis suite, and at the CNR–IGG Institute

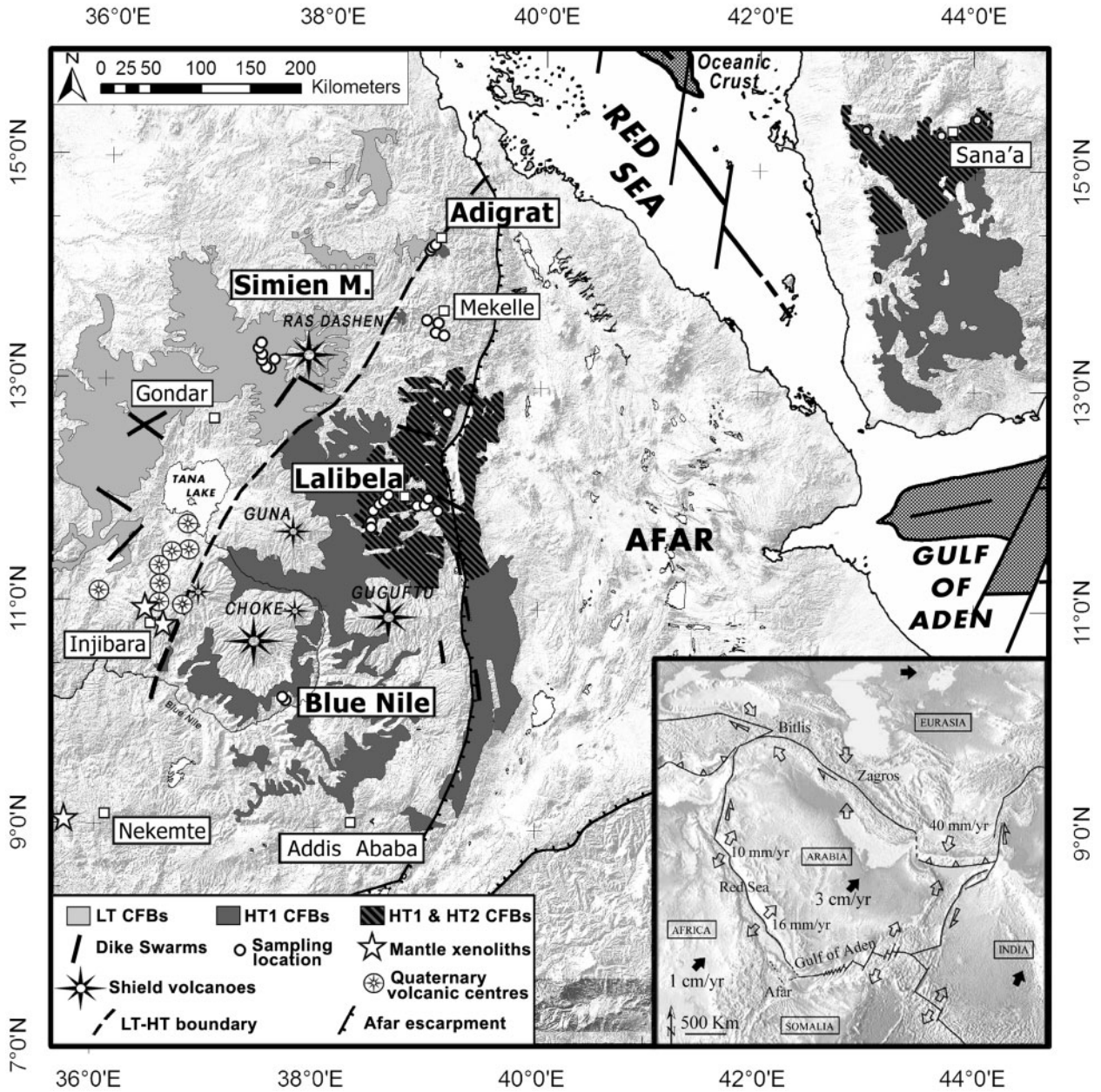

Fig. 1. Sketch map of the Oligocene continental flood basalts (CFBs) of the Northern Ethiopia and the Yemen conjugate margins, based on the geological map by Merla *et al.* (1973), NASA STRM images, data from Baker *et al.* (1996), Pik *et al.* (1998), Kieffer *et al.* (2004) and this work. LT, Low-Ti tholeiitic basalts; HT1, High-Ti tholeiitic basalts; HT2, very High-Ti transitional basalts and picrites. Dyke swarms after Mège & Korme (2004); locations of mantle xenoliths hosted in Quaternary alkaline volcanic rocks in the plateau area are also indicated. Inset: regional geodynamic sketch map with plate motions and velocities after Bellahsen *et al.* (2003).

of Padova using a Cameca-Camebax electron microprobe, fitted with three wavelength-dispersive spectrometers, using natural silicates and oxides as standards.

Trace element analyses of clinopyroxenes were carried out at the CNR–IGG of Pavia by laser ablation microanalysis (LAM) ICP-MS, using an Elan DRC-e mass spectrometer coupled with a Q-switched Nd:YAG laser source (Quantel Brilliant). The CaO content was used as an internal standard. Precision and accuracy, better than 10% for concentrations at ppm level, were assessed by repeated analyses of NIST SRM 612 and BCR-2 standards.

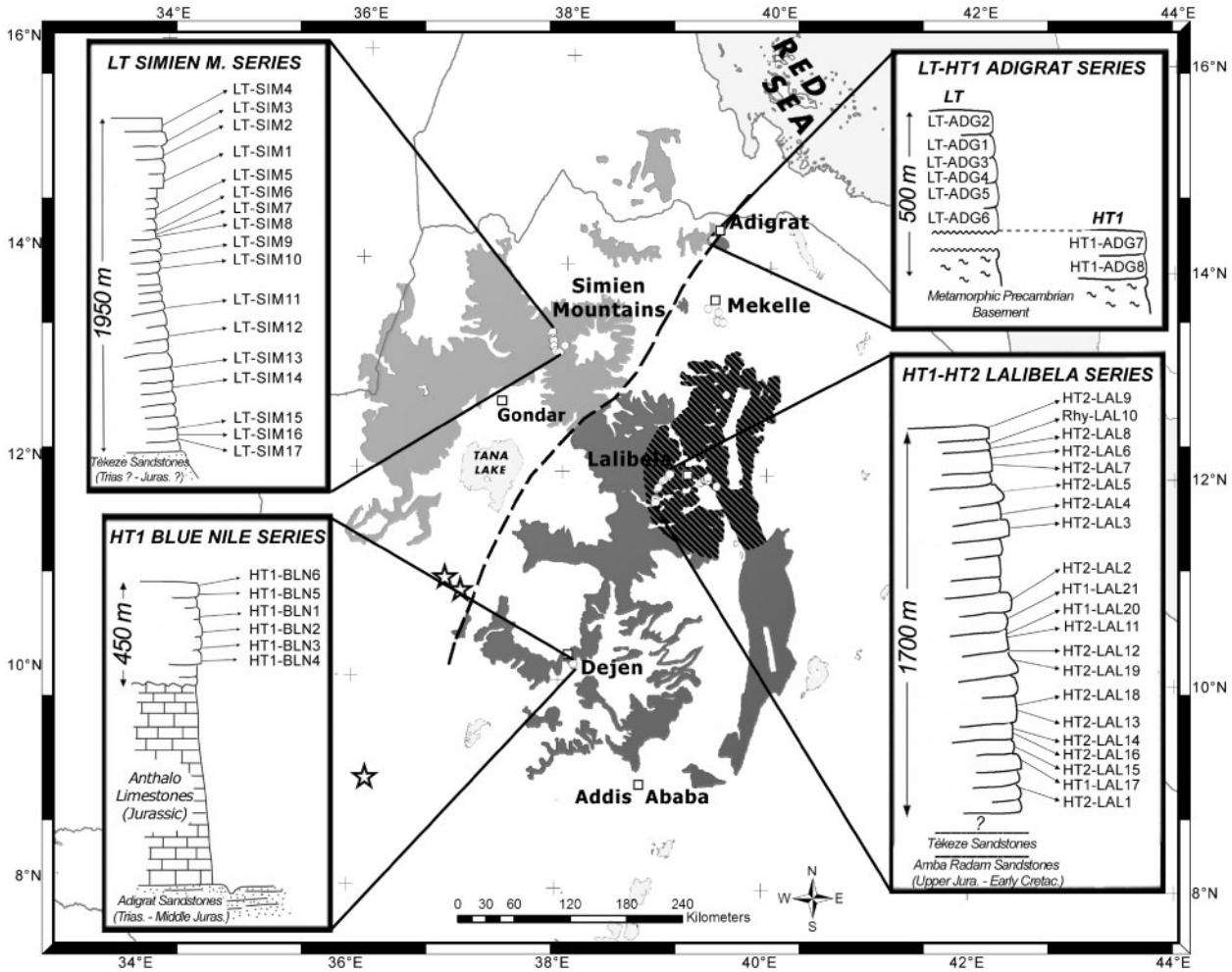

Fig. 2. Generalized cross-sections and sampling locations of Oligocene CFBs within the Northern Ethiopian plateau. The thickness of the lava pile overlying the basement is indicated. Rhy, rhyolite flow. Other abbreviations and symbols as in Fig. 1.

PETROGRAPHY, CLASSIFICATION AND MINERAL CHEMISTRY

Northern Ethiopia CFBs

The new major and trace element analyses of the Northern Ethiopian plateau basalts (Table 1 and Figs 3 and 4) confirm the existence of three main magma types spatially zoned according to their TiO_2 content (Pik *et al.*, 1998) and allow a more precise definition of their zonal arrangement (Figs 1 and 2): Low-Ti tholeiites (LT), in the NW, are quantitatively predominant (150 000 km^3); High-Ti lavas (HT1) predominate southeastwards; ultra-titaniferous transitional basalts and picrites (HT2) are concentrated in the Lalibela area, closer to the centre of the Afar triangle.

In both alkali vs silica (Fig. 3) and TiO_2 vs MgO (Fig. 4) diagrams distinctive compositional features of the three magma types can be observed: LT basalts mostly plot in the subalkaline field, showing the widest differentiation range with MgO 3–12 wt %, coupled with the lowest TiO_2 contents (1·0–3·5 wt %); the HT1 group is mainly composed of tholeiitic basalts with MgO 4–9 wt % and TiO_2 2·5–4·8 wt %; HT2 transitional basalts and picrites cluster around the alkaline–subalkaline boundary (Fig. 3) with MgO 5–12 wt % and TiO_2 3·5–5·9 wt % for basalts, and MgO 13–16 wt % and TiO_2 2·6–4·5 wt % for picrites. Moreover, there is a broad correlation between TiO_2 and $Fe_2O_{3\ tot}$, the latter increasing from 11–12 wt % in the least differentiated LT to 14–15 wt % in the HT lavas (not shown).

The decreasing silica saturation from LT to HT2 is reflected by the parallel decrease in normative hypersthene from 12–23% in LT and HT1 tholeiites to ≤10% in many HT2 transitional basalts and picrites.

CFBs from the coeval Yemen plateau (Manetti *et al.*, 1991; Baker *et al.*, 1996; authors' unpublished data) are classified as HT1 and HT2, and show striking compositional

Table 1: Bulk-rock major and trace element analyses of Northern Ethiopian CFBs

Rock type:	LT-Bas	LT-Bas	LT-Bas	LT-Bas	LT-Bas	LT-Bas	LT-Bas	HT1-Bas	HT1-Bas	HT1-Bas	HT1-Bas
Locality:	Simien	Simien	Simien	Simien	Adigrat	Adigrat	Adigrat	Adigrat	Adigrat	B. Nile	B. Nile
Longitude:	37°57′04″	37°53′11″	37°51′15″	37°52′36″	39°24′50″	39°25′10″	39°25′52″	39°25′39″	39°25′25″	38°09′59″	38°10′08″
Latitude:	13°08′33″	13°12′01″	13°16′41″	13°20′23″	14°15′31″	14°15′30″	14°15′52″	14°16′17″	14°16′22″	10°08′29″	10°08′16″
Sample:	SIM2	SIM7	SIM15	SIM17	ADG3	ADG4	ADG6	ADG7	ADG8	BLN2	BLN4
SiO_2	50·09	49·55	47·16	49·36	45·10	44·99	48·52	42·20	41·87	49·94	48·67
TiO_2	3·31	1·70	1·33	1·52	1·45	1·31	1·48	4·77	4·68	3·23	3·09
Al_2O_3	14·62	17·19	15·38	16·18	15·34	16·63	17·59	12·85	12·78	13·00	14·62
$Fe_2O_{3\ Tot}$	14·81	10·78	10·78	11·97	12·55	12·04	10·96	18·05	17·84	13·62	14·64
MnO	0·20	0·13	0·16	0·16	0·14	0·16	0·16	0·16	0·16	0·22	0·17
MgO	3·77	5·41	9·23	7·38	12·13	10·44	7·38	8·42	9·27	5·14	5·29
CaO	8·51	10·82	10·33	9·75	8·40	9·96	9·91	6·72	6·56	9·64	10·15
Na_2O	3·47	2·57	2·47	2·63	1·50	1·83	2·78	3·28	3·39	3·00	2·39
K_2O	0·86	0·33	0·33	0·38	0·27	0·17	0·21	0·60	0·63	0·69	0·72
P_2O_5	0·36	0·16	0·18	0·23	0·20	0·17	0·20	0·69	0·63	0·84	0·20
LOI	0·00	1·36	2·64	0·44	2·93	2·30	0·82	2·28	2·19	0·67	0·04
mg-no.	0·36	0·53	0·66	0·58	0·68	0·66	0·60	0·51	0·54	0·46	0·45
Ni (ppm)	n.d.	89	150	106	78	202	51	68	114	4	80
Co	37	36	45	46	48	62	46	50	54	31	40
Cr	18	203	82	65	168	319	81	40	41	67	128
V	443	250	222	234	225	230	270	267	310	330	369
Sc	39	26	28	25	25	31	28	15	17	36	33
Sr	338	345	343	429	250	344	268	1211	868	568	438
Ba	386	153	168	288	105	76	79	255	218	788	195
Zr	203	110	94	131	95	98	100	375	319	170	235
Hf	5·88	3·08	2·36	2·86	2·57	2·75	2·52	9·59	8·69	4·15	5·65
Nb	13·6	8·63	5·06	6·74	5·14	4·72	4·81	19·0	17·3	18·8	25·2
Ta	0·63	0·78	0·06	0·15	0·44	0·50	0·51	1·17	0·98	1·03	1·43
Th	1·77	0·69	0·45	0·67	0·40	0·29	0·22	1·27	1·14	2·11	2·17
U	0·42	0·23	0·10	0·14	0·06	0·13	0·13	0·21	0·28	0·61	0·54
Y	49·2	25·1	21·4	26·2	22·6	25·8	12·0	22·8	21·4	36·5	32·3
La	18·0	8·86	6·05	9·91	5·95	4·00	4·05	20·7	18·8	27·4	22·2
Ce	41·5	23·1	14·9	23·0	15·2	12·4	14·3	54·4	49·5	61·8	50·4
Pr	5·67	3·23	2·25	3·24	2·51	2·09	1·79	8·73	7·98	8·94	6·72
Nd	28·2	15·3	11·3	16·1	12·6	11·5	8·98	44·9	40·4	44·9	32·0
Sm	6·85	4·12	3·02	3·52	3·43	3·75	2·43	11·1	9·48	9·36	7·36
Eu	2·35	1·43	1·30	1·57	1·36	1·39	0·82	3·39	3·01	3·68	2·30
Gd	7·36	4·97	2·85	3·87	3·18	4·56	2·78	8·32	7·66	8·87	6·59
Tb	1·49	0·83	0·62	0·86	0·66	0·79	0·46	1·26	1·18	1·33	1·10
Dy	7·82	4·88	3·42	4·41	3·87	4·80	2·67	5·59	5·29	6·92	5·73
Ho	1·58	0·96	0·68	0·84	0·75	0·97	0·53	0·78	0·70	1·19	1·05
Er	4·27	2·70	1·94	2·34	2·23	2·81	1·48	1·81	1·65	3·30	2·87
Tm	0·57	0·36	0·28	0·33	0·32	0·38	0·20	0·18	0·19	0·43	0·34
Yb	3·77	2·18	1·76	2·14	2·08	2·36	1·18	1·07	0·91	2·62	2·32
Lu	0·51	0·30	0·26	0·28	0·26	0·34	0·16	0·15	0·14	0·37	0·35

(continued)

Table 1: Continued

Rock type:	HT1-Bas	HT2-Bas	HT2-Bas	HT2-Pi	HT2-Pi	HT2-Pi	HT2-Pi*	HT2-Bas	HT2-Bas	HT2-Bas	HT2-Bas
Locality:	Lalibela	Lalibela	Lalibela	Lalibela	Lalibela	Lalibela	Lalibela	Lalibela	Lalibela	Lalibela	Lalibela
Longitude:	38°55′20″	39°30′56″	39°25′39″	39°25′12″	39°24′20″	39°23′42″	39°03′04″	39°00′14″	38°59′10″	38°54′45″	38°55′09″
Latitude:	11°43′19″	11°53′13″	11°58′27″	11°57′59″	11°57′13″	11°56′39″	12°00′21″	11°56′42″	11°56′01″	11°45′52″	11°45′02″
Sample:	LAL20	LAL1	LAL3	LAL5	LAL6	LAL9	LAL11	LAL14	LAL15	LAL18	LAL19
SiO_2	49·82	47·52	50·02	46·02	45·10	46·25	44·22	45·64	45·23	50·15	49·91
TiO_2	3·51	5·44	3·92	4·51	4·02	3·44	3·02	5·91	5·50	3·87	4·01
Al_2O_3	13·28	8·05	10·99	8·59	8·30	8·76	6·19	7·78	9·22	13·46	13·38
$Fe_2O_{3\ Tot}$	14·59	12·76	13·05	13·39	13·94	14·07	11·61	15·04	15·06	14·32	14·41
MnO	0·21	0·17	0·17	0·19	0·18	0·18	0·17	0·17	0·19	0·18	0·19
MgO	4·58	10·32	8·08	13·00	16·20	14·41	25·10	11·97	9·27	4·85	5·00
CaO	9·11	11·68	9·74	10·03	9·25	10·28	6·10	9·83	10·32	8·70	8·93
Na_2O	3·13	2·00	2·40	1·89	1·73	1·53	0·56	1·95	2·91	2·86	2·85
K_2O	1·02	1·30	1·27	0·96	0·74	0·79	0·87	1·17	1·17	1·20	0·96
P_2O_5	0·75	0·61	0·36	0·41	0·40	0·29	0·35	0·52	0·49	0·41	0·36
LOI	0·00	0·16	0·00	1·00	0·16	0·00	1·82	0·02	0·64	0·00	0·00
mg-no.	0·41	0·65	0·58	0·69	0·72	0·70	0·83	0·64	0·58	0·43	0·44
Ni (ppm)	n.d.	237	233	646	1097	697	1373	611	214	49	50
Co	28	45	48	67	71	71	96	59	56	33	30
Cr	24	595	494	808	1551	1203	1295	814	478	73	71
V	383	475	400	449	371	343	281	482	513	352	372
Sc	31	53	41	44	43	43	31	50	43	30	34
Sr	508	596	516	457	470	392	304	684	673	562	572
Ba	542	377	426	336	259	253	641	369	507	372	368
Zr	199	436	320	309	265	249	176	495	442	358	358
Hf	5·72	12·8	8·17	8·72	6·68	6·15	5·74	14·3	12·5	10·1	12·6
Nb	31·5	67·0	43·7	45·0	36·5	34·8	28·7	59·8	91·7	65·4	76·37
Ta	1·94	4·03	2·68	2·66	2·10	2·11	1·64	3·58	7·10	7·99	4·62
Th	2·62	4·37	4·48	3·68	2·72	2·41	2·32	5·33	6·73	4·80	5·97
U	0·98	1·39	1·59	0·93	0·60	0·81	0·64	1·67	2·11	1·84	2·30
Y	34·4	41·8	30·0	34·1	27·7	25·1	23·1	50·6	39·7	38·6	49·4
La	26·0	47·5	37·7	36·0	28·3	60·8	22·8	49·0	61·2	37·2	46·4
Ce	63·3	113	80·5	81·4	65·9	58·3	53·0	115	142	86·0	107
Pr	8·49	15·2	10·7	11·04	8·80	7·57	6·84	16·2	18·2	11·0	13·7
Nd	39·7	68·9	45·1	51·1	41·2	33·9	33·3	79·9	77·6	48·1	60·2
Sm	8·76	15·3	9·64	10·8	8·58	7·63	6·51	17·0	15·5	10·3	13·0
Eu	3·00	4·45	2·79	3·03	2·53	2·27	2·24	4·80	4·50	3·02	3·83
Gd	8·47	14·6	9·52	8·83	7·01	7·65	6·04	14·0	14·5	9·92	12·5
Tb	1·44	1·95	1·31	1·37	1·10	1·07	1·00	2·12	1·85	1·67	2·13
Dy	6·57	9·46	6·62	6·81	5·47	5·47	4·83	10·3	8·87	7·45	9·44
Ho	1·33	1·59	1·17	1·08	0·88	0·97	0·73	1·65	1·50	1·46	1·86
Er	3·32	4·01	3·06	2·80	2·27	2·51	2·00	4·29	3·79	3·58	4·56
Tm	0·51	0·47	0·38	0·34	0·27	0·31	0·26	0·46	0·44	0·54	0·70
Yb	2·84	2·64	2·19	2·06	1·63	1·79	1·43	2·94	2·50	2·97	3·77
Lu	0·42	0·34	0·29	0·24	0·23	0·24	0·20	0·39	0·33	0·43	0·55

LT-Bas, Low-Ti tholeiitic basalt; HT1-Bas, High-Ti tholeiitic basalt; HT2-Bas, very High-Ti transitional basalt; HT2-Pi, very High-Ti picrite. mg-number = mol MgO/(MgO + FeO) with wt % Fe_2O_3/FeO = 0·15; n.d., not detected; LOI, loss on ignition.
*Cumulus olivine.

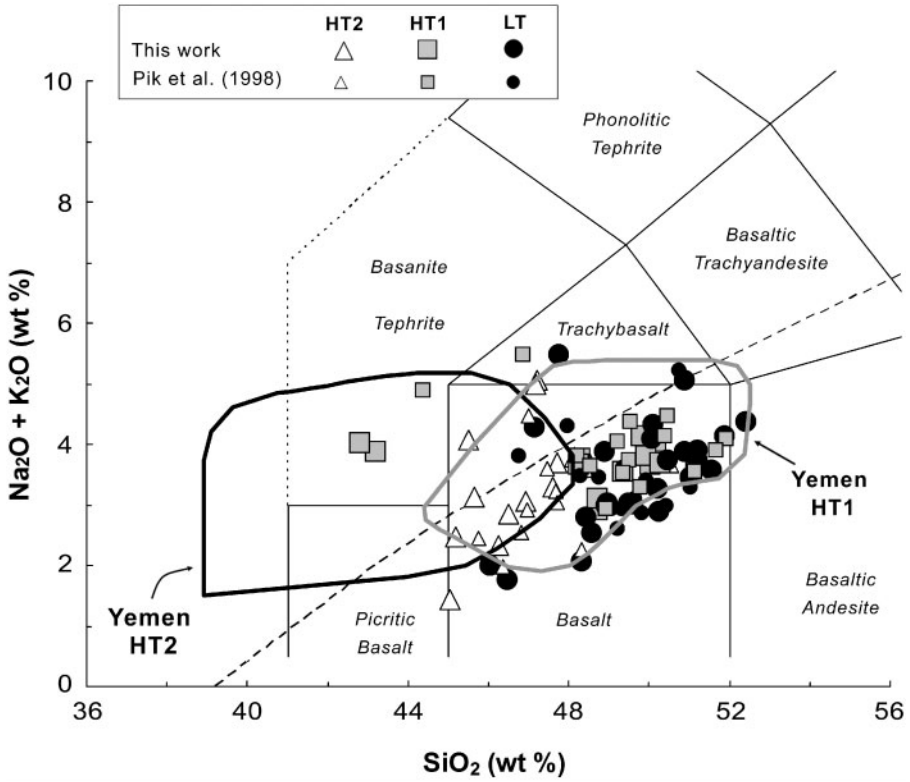

Fig. 3. Total alkali–silica classification diagram (Le Bas *et al.*, 1992) for the Northern Ethiopia CFBs (data from this work and Pik *et al.*, 1998). For comparison, data from coeval Yemen CFBs have also been plotted (from Baker *et al.*, 1996; and authors' unpublished data). LT, Low-Ti tholeiites; HT1, High-Ti tholeiites; HT2, very High-Ti transitional basalts and picrites. The dashed line dividing alkalic and subalkalic series is after Irvine & Baragar (1971).

similarities to the Northern Ethiopian High-Ti lavas facing the Afar triangle (Figs 3 and 4). This further supports the hypothesis that, before the opening of the Afar–Red Sea system, these volcanic districts would have been part of the same magmatic province extending ~700 km in an east–west direction. A regional comparison shows that the LT and HT1 lavas from the Ethiopia–Yemen province show close similarities to other Low- and High-Ti CFB provinces (e.g. Paranà, Piccirillo & Melfi, 1988; Deccan, Melluso *et al.*, 1995). On the other hand, the distinctive compositions of the HT2 ultra-titaniferous basalts and picrites seem to be only partially comparable with those of some picrites from the Karoo igneous province (Sweeney *et al.*, 1991; Cawthorn & Biggar, 1993; Ellam, 2006) and the Siberian Traps (meymechites: Campbell *et al.*, 1992).

The petrographic characteristics of the various lava types are summarized in Table 2. Low-Ti basalts (Fig. 5a) are hypocrystalline to microcrystalline to doleritic, with a porphyritic index varying in the range 0–10% in most samples. Phenocrysts mainly consist of dominant plagioclase and scarce olivine in both the Simien Mountains and Adigrat sequences. The groundmass is locally sub-ophitic with plagioclase laths, interstitial clinopyroxene and abundant magnetite and ilmenite microcrystals; brownish interstitial glass is occasionally present. This crystallization order is typical of tholeiitic melts. Doleritic samples from the Adigrat suite often show several generations of olivine and plagioclase crystals, most probably attributable to multiple magma injections in a subvolcanic setting.

HT1 basalts (Fig. 5b and c) are mainly aphyric with variable grain size. Sub-ophitic to doleritic (Adigrat samples) textures appear holocrystalline, coarse-grained, with plagioclase laths, poikilitic (pinkish) clinopyroxene and small magnetite crystals sometimes associated with rare phlogopite. This paragenesis is consistent with the slightly more alkaline and hydrated character of HT1 with respect to the LT magmas. Samples from the Blue Nile area and the lower part of the Lalibela sequence are aphyric and fine-grained, with olivine microphenocrysts (generally iddingsitized), skeletal swallow-tail plagioclase laths, skeletal clinopyroxene and ilmenite crystals, magnetite grains and clear yellowish glass in the interstices.

HT2 basalts and picrites (Fig. 5d–f) from the Lalibela sequence are always porphyritic in texture with

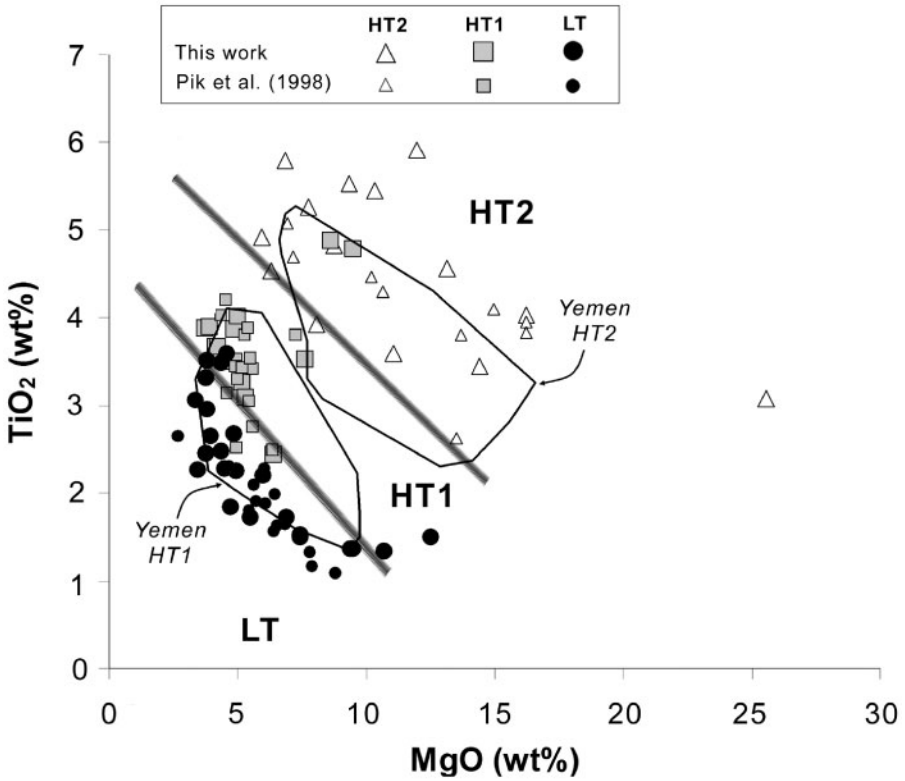

Fig. 4. TiO_2 vs MgO (wt %) for the Northern Ethiopian CFBs (data from this study and Pik *et al.*, 1998). For comparison data from coeval Yemeni CFBs have also been plotted (from Baker *et al.*, 1996; and authors' unpublished data). LT, Low-Ti tholeiites; HT1, High-Ti tholeiites; HT2, very High-Ti transitional basalts and picrites. Empirical intergroup boundaries are drawn to minimize misclassified samples.

Table 2: Petrographic characteristics of Northern Ethiopian CFBs

Rock type	mg-no. range	Phenocryst and microphenocryst	Groundmass
LT tholeiites	68–36	Pl, ± Ol ± Cr-Sp, ± Cpx	Pl, Cpx, Fe–Ti Ox, ± Gl
HT1 tholeiites	59–34	±(Ol)	Pl, Cpx, Fe–Ti Ox, ± Gl
HT2 transitional basalts	69–48	Ol ± Cr-Sp, Cpx, ± Pl	Cpx, Pl, Fe–Ti Ox, Af, ± Phlog
HT2 picrites	72–68*	Ol ± Cr-Sp, Cpx	Cpx, Pl, Fe–Ti Ox, Af, ± Gl

Ol, olivine; Cpx, clinopyroxene; Pl, plagioclase; Af, alkali feldspar; Phlog, phlogopite; Cr-Sp, Cr-spinel; Fe–Ti Ox, Ti-magnetite and ilmenite; Gl, glass. Completely altered minerals are in parentheses. Other abbreviations as in Table 1.*Picrites with evidence of cumulus olivine are excluded.

phenocrysts of olivine, sometimes including cr-spinel, pinkish Ti-rich clinopyroxene (up to 5 mm across) and rare plagioclase. The groundmass is microcrystalline to hypocrystalline, and is made up of the same phenocryst phases plus Ti-magnetite, scarce phlogopite and alkali feldspar. A few picrites are not representative of liquid compositions, being olivine cumulative (e.g. LAL11, with modal olivine up to 30–35%) and reaching extremely high mg-number (0·83).

Representative compositions of the main mineral phases are reported in Tables 3–6 and Figs 6 and 7. These mineral data, integrated with those from Pik *et al.* (1998), are discussed below.

Olivine (Table 3 and Fig. 6c) varies in composition in the different magma types: $Fo_{81–77}$ and NiO from 0·20 to 0·06 wt % in LT tholeiites; $Fo_{75–51}$ in HT1 tholeiites; $Fo_{87–77}$ and NiO from 0·37 to 0·18 wt % in HT2 transitional basalts; $Fo_{90–85}$ and NiO from 0·50 to 0·33 wt % in HT2 picrites.

Cr-spinel microcrysts (Table 3), often included in olivine phenocrysts, show an increase in Cr_2O_3 and TiO_2 and a decrease in Al_2O_3 content from LT to HT2 basalts and

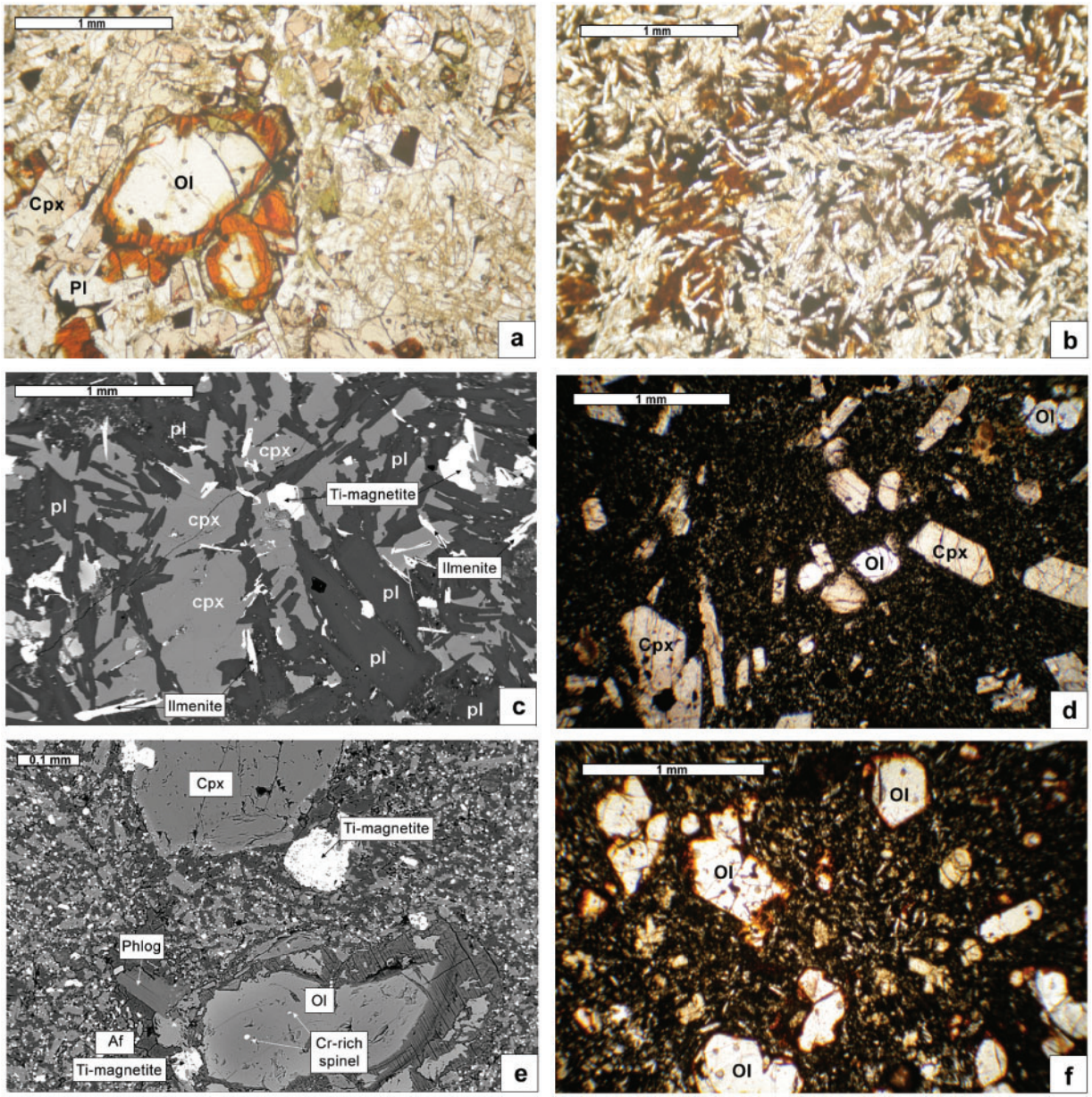

Fig. 5. Photomicrographs of Northern Ethiopian CFBs. (a) LT basalt showing porphyritic texture with olivine phenocrysts in a sub-ophitic groundmass. (b) HT1 basalt with aphyric texture showing small plagioclase laths, interstitial clinopyroxene, Fe–Ti oxides and minor glass. (c) Scanning electron micrograph of HT1 basalt with aphyric sub-ophitic texture showing plagioclase laths, interstitial clinopyroxene and Fe–Ti oxides. (d) HT2 basalt with porphyritic texture bearing clinopyroxene and olivine phenocrysts in a microcrystalline to hypocrystalline groundmass. (e) Scanning electron micrograph of HT2 basalt showing phenocrysts of olivine (including small Cr-rich spinels) and clinopyroxene, set in a microcrystalline groundmass made up of olivine, clinopyroxene, plagioclase, Fe–Ti oxide and minor phlogopite and alkali feldspar. (f) HT2 picrite showing porphyritic texture with phenocrysts of euhedral olivine and minor clinopyroxene set in a microcrystalline groundmass.

picrites, parallel to their bulk-rock compositions. These characteristics closely fit the mineralogical characteristics of mantle-derived near-primary magmas (Larsen & Pedersen, 2000).

Clinopyroxenes are mainly augitic in composition (Table 4 and Fig. 6a), showing a general intra-group ferrosilite (Fs) increase from phenocryst to groudmass. As shown in Fig. 6b, the TiO_2 content is lower in LT than in HT, reflecting the original differences between the distinct magma types. In addition to Fs, an intra-group TiO_2 increase occurs from early to late crystallizing clinopyroxenes, reflecting the common fractional crystallization trend of tholeiitic CFB series (Bellieni *et al.* 1984).

Table 3: Representative analyses of olivine and included Cr-spinel from Northern Ethiopian CFBs

Rock type:	LT-Bas								HT1-Bas				HT2-Bas					
Sample:	ADG4								LAL20				LAL3				LAL8	
Mineral:	Ol4b Ph-c	Ol4a Ph-r	Ol6b Ph-c	Ol6a Ph-r	Cr-Sp1 (in Ol6)	Cr-Sp2 (in Ol6)	Ol7a-c Ph-c	Ol7b-r Ph-r	Ol1a Gm	Ol1b Gm	Ol2a Gm	Ol2b Gm	Ol1 Ph-c	Cr-Sp1 (in Ol1)	Ol2 Ph-c	Cr-Sp2 (in Ol2)	Ol1b Ph-c	Ol2b Ph-c
SiO_2	40·24	39·53	40·36	39·65	—	—	40·46	39·78	36·87	36·64	35·06	36·29	40·38	—	39·50	—	41·58	40·04
TiO_2	0·08	0·01	—	—	0·95	0·59	—	0·05	—	—	—	—	—	2·84	—	4·92	—	0·06
Al_2O_3	0·02	0·03	0·08	0·03	38·00	42·44	0·02	0·02	—	—	—	—	—	7·73	—	10·25	0·04	0·02
FeO_{Tot}	17·94	20·18	17·15	19·17	21·98	20·16	18·46	21·05	31·99	34·88	40·00	31·90	12·18	29·35	12·51	25·78	11·88	17·65
MnO	0·20	0·22	0·23	0·33	—	—	0·31	0·33	0·56	0·75	0·74	0·61	—	—	—	—	0·20	0·32
MgO	41·58	40·72	42·24	41·07	13·73	14·82	41·05	40·89	31·03	28·02	23·63	30·30	47·40	8·51	45·70	9·00	46·76	41·79
CaO	0·35	0·35	0·34	0·32	—	—	0·36	0·31	0·32	—	0·31	0·29	0·31	—	0·28	—	0·20	0·35
Na_2O	—	—	0·03	—	—	—	0·03	—	—	—	—	—	—	—	—	—	—	—
K_2O	0·01	—	—	—	—	—	—	—	—	—	—	—	—	—	—	—	—	—
Cr_2O_3	0·03	0·02	0·01	0·02	23·58	19·67	0·10	—	—	—	—	—	—	47·51	—	42·78	0·10	—
NiO	0·13	0·19	0·20	0·16	—	—	0·06	0·08	—	—	—	—	—	—	0·34	—	0·32	0·37
V_2O_5	—	—		—	0·47	0·47	—	—	—	—	—	—	—	—	—	—	—	—
Total	100·58	101·27	100·64	100·74	98·71	98·16	100·86	101·25	100·77	100·29	99·74	99·39	100·27	95·92	98·34	92·74	101·08	100·60
mg-no.	0·80	0·78	0·81	0·79	0·64	0·62	0·80	0·77	0·63	0·59	0·51	0·63	0·87	0·41	0·87	0·42	0·87	0·81
cr-no.					0·29	0·24								0·81		0·74		

Rock type:	HT2-Bas						HT2-Pi											
Sample:	LAL14				LAL15		LAL5			LAL6							LAL9	
Mineral:	Ol4b Ph-c	Ol4a Ph-c	Ol1 Ph-c	Cr-Sp1 (in Ol1)	Ol112 Ph-c	Ol83 Ph-c	Ol4a Ph-c	Ol3a Ph-r	Ol3b Ph-c	Ol2a Ph-c	Ol2b Ph-r	Cr-Sp1 (in Ol2)	Ol2d Ph-c	Ol1b Ph-c	Cr-Sp1 (in Ol1)	Ol5a Ph-c	Ol5b Ph-c
SiO_2	40·64	40·92	37·71	—	40·63	40·13	41·11	40·04	40·68	41·03	40·62		41·68	40·69	—	40·97	41·54
TiO_2	0·02	0·01	—	10·60	0·04	0·07	0·04	0·02	0·08	0·07	0·02	2·74	0·01	0·07	3·90	0·05	—
Al_2O_3	0·01	—	—	6·60	0·05	0·03	0·02	—	0·05	0·03	0·05	7·58	0·03	0·06	6·69	0·02	—
FeO_{Tot}	12·49	13·30	21·03	51·03	14·70	17·11	10·36	13·97	11·91	9·55	12·49	27·11	10·03	13·63	39·74	10·92	11·13
MnO	0·22	0·20			0·05	0·27	0·16	0·22	0·09	0·14	0·17		0·11	0·17	—	0·20	0·11
MgO	45·82	46·26	39·70	4·72	45·20	42·29	47·75	45·16	47·15	49·05	46·73	9·41	48·02	45·65	6·57	48·08	47·63
CaO	0·35	0·31	0·28	—	0·29	0·29	0·29	0·33	0·28	0·25	0·27		0·27	0·23	—	0·37	0·33
Na_2O	0·04	—	—	—	—	0·04	—	—	0·04	0·04	—		0·02	0·03	—	0·05	0·01
K_2O	0·02	—	—	—	—	—	—	—	—	0·02	0·01		—	0·03	—	—	0·01
Cr_2O_3	0·06	0·01	—	18·53	0·07	—	0·08	0·07	0·07	0·15	0·10	47·53	0·09	0·03	41·00	0·05	0·09
NiO	0·36	0·18	0·33	—	0·33	0·18	0·35	0·37	0·35	0·41	0·39		0·39	0·41	—	0·50	0·33
V_2O_5	—	—	—	0·67	—	—	—	—	—	—	—	—	—		—	—	—
Total	100·04	101·19	99·05	92·15	101·36	100·41	100·16	100·19	100·70	100·74	100·84	94·37	100·65	101·00	97·90	101·21	101·17
mg-no.	0·87	0·86	0·77	0·20	0·85	0·81	0·89	0·85	0·88	0·90	0·87	0·46	0·89	0·86	0·31	0·89	0·88
cr-no.				0·65								0·81			0·80		

Ph, phenocryst; Gm, groundmass; c, core; r, rim; —, not detected. For the same sample, numbers refer to different crystals, letters to different analyses. mg-number = Mg/(Fe + Mg) and cr-number = Cr/(Al + Cr) from a.f.u. Other abbreviations as in Tables 1 and 2.

Table 4: Representative analyses of clinopyroxene from Northern Ethiopian CFBs

Rock type:	LT-Bas											HT1-Bas			HT2-Bas					
Sample:	ADG4				ADG3				SIM7			LAL20			LAL1		LAL3			
Mineral:	Cpx-2a Gm	Cpx-2b Gm	Cpx-5b Gm	Cpx-5c Gm	Cpx-1a Gm	Cpx-1b Gm	Cpx-2a Gm	Cpx-2b Gm	Cpx-D4 Ph	Cpx-D3 Ph	Cpx-D1 Gm	Cpx-2 Gm	Cpx-8 Gm	Cpx-1 Gm	Cpx-1 Ph-c	Cpx-3 Gm	Cpx-1 Ph-c	Cpx-2 Ph-c	Cpx-3 Gm	Cpx-5 Gm
SiO_2	49·78	50·70	51·48	50·84	50·49	48·60	49·73	49·66	52·36	51·90	52·01	51·33	51·11	49·42	51·81	50·11	52·18	51·65	49·01	48·41
TiO_2	2·09	1·54	1·55	1·92	1·73	2·17	2·48	2·10	0·53	0·67	0·63	1·30	1·73	2·05	1·43	1·84	0·93	1·11	2·42	2·88
Al_2O_3	3·55	3·74	2·45	3·24	3·57	3·97	3·10	3·44	2·52	2·85	1·52	1·65	2·36	2·88	1·43	2·34	1·39	1·89	3·39	4·03
FeO_{Tot}	9·06	7·05	9·50	8·85	8·24	10·79	12·39	9·92	6·72	6·61	9·07	11·95	11·07	11·56	5·83	8·75	5·45	6·02	10·06	8·19
MnO	0·20	0·19	0·19	0·19	0·21	0·23	0·32	0·28	—	—	0·32	0·35	—	—	—	—	—	—	0·34	—
MgO	13·75	14·03	13·90	13·56	13·81	12·59	12·06	13·12	17·28	16·79	17·13	15·18	14·30	13·97	17·06	15·36	18·32	17·35	15·07	14·86
CaO	20·85	21·36	21·19	21·32	21·55	20·41	19·58	20·77	19·58	20·12	17·50	18·27	19·73	18·52	21·61	19·89	19·65	20·25	18·23	19·84
Na_2O	0·35	0·42	0·38	0·52	0·27	0·48	0·48	0·41	0·44	0·54	0·45	—	0·51	0·56	0·43	0·45	—	—	0·39	0·41
K_2O	—	0·01	—	—	0·01	0·01	—	—	—	—	—	—	—	—	—	—	—	—	—	—
Cr_2O_3	0·05	0·56	—	—	0·15	—	0·02	—	0·62	0·80	—	—	—	—	0·38	—	0·77	0·51	0·49	0·52
NiO	0·06	—	—	—	—	0·08	—	0·10	—	—	—	—	—	—	—	—	—	—	—	—
Total	99·68	99·60	100·64	100·44	100·03	99·25	100·17	99·70	100·06	100·29	98·63	100·03	100·80	98·96	99·98	98·74	98·70	98·78	99·41	99·14
mg-no.	0·73	0·78	0·72	0·73	0·75	0·68	0·63	0·70	0·82	0·82	0·77	0·69	0·70	0·68	0·84	0·76	0·86	0·84	0·73	0·76

Rock type:	HT2-Bas								HT2-Pi								
Sample:	LAL8		LAL14						LAL5			LAL6				LAL9	
Mineral:	Cpx-3A Ph-r	Cpx-3B Ph-c	Cpx-3a Ph-c	Cpx-3b Ph-c	Cpx-3c Ph-r	Cpx-3d Ph-c	Cpx-1 Gm	Cpx-2 Gm	Cpx-1B Ph-c	Cpx-2A Ph-c	Cpx-2B Ph-c	Cpx-2 Gm	Cpx-1 Gm	Cpx-AB2 Gm	Cpx-AB Gm	Cpx-2b Ph-c	Cpx-4a Ph-c
SiO_2	51·73	52·28	51·90	51·66	51·85	51·39	50·47	48·75	51·98	51·01	51·55	51·06	51·49	45·31	46·92	53·50	53·16
TiO_2	1·26	1·26	1·20	1·29	1·28	1·39	1·66	2·54	1·43	1·72	1·74	1·64	1·69	4·62	3·46	0·73	0·87
Al_2O_3	2·19	2·19	1·76	2·13	1·81	1·06	2·32	3·09	2·31	3·04	2·86	2·38	2·58	6·54	4·87	1·42	1·85
FeO_{Tot}	6·07	5·80	7·74	6·86	6·69	5·74	9·53	9·01	6·21	6·16	6·35	6·23	6·28	10·44	10·32	4·88	5·93
MnO	0·16	0·09	0·11	0·12	0·09	—	—	—	0·07	0·16	0·07	—	—	—	—	0·05	0·13
MgO	16·52	16·52	15·20	15·40	15·52	16·85	14·67	15·16	15·97	15·20	15·56	16·30	16·46	12·79	14·30	17·66	16·89
CaO	21·15	20·83	21·17	21·32	21·64	21·37	20·04	19·56	21·07	21·37	20·97	21·64	21·52	20·15	20·02	21·92	21·20
Na_2O	0·38	0·30	0·33	0·35	0·31	0·47	—	0·44	0·26	0·40	0·34	0·42	0·49	0·54	—	0·22	0·27
K_2O	0·02	—	0·04	0·01	0·01	—	—	—	—	0·01	0·01	—	—	—	—	—	0·01
Cr_2O_3	0·56	0·60	—	0·15	0·15	0·37	—	—	0·55	0·43	0·45	0·84	0·78	—	—	0·82	0·59
NiO	—	0·10	—	0·08	—	—	—	—	—	—	—	—	—	—	—	0·14	0·05
Total	100·03	99·89	99·44	99·29	99·35	98·64	98·68	98·55	99·86	99·50	99·90	100·50	101·30	100·39	99·90	101·20	100·90
mg-no.	0·83	0·84	0·78	0·80	0·81	0·84	0·73	0·75	0·82	0·81	0·81	0·82	0·82	0·69	0·71	0·87	0·84

For the same sample, numbers refer to different crystals, letters to different analyses. Other abbreviations as in Tables 1–3.

Feldspar is represented by ubiquitous plagioclase varying from $An_{81–50}$ in LT basalts to $An_{63–44}$ in HT1 and $An_{53–35}$ in HT2 basalts and picrites (Table 5 and Fig. 7). Alkali-feldspar ($Ab_{58–43}$–$Or_{29–53}$) and scarce phlogopite (Table 5) are mainly observed in the groundmass of HT2 lavas, supporting the progressive increase of alkalinity and H_2O content from LT to HT2 magmas.

Fe–Ti oxides (Table 6), consisting of Ti-rich magnetite (ulvöspinel 22–68%) and ilmenite, are ubiquitous phases

Table 5: Representative analyses of Fe–Ti oxide from Northern Ethiopian CFBs

Rock type:	LT-Bas						HT1-Bas						HT2-Bas		
Sample:	ADG4			SIM7			LAL20						LAL1		
Mineral:	Ilm-1 Gm	Ilm-2 Gm	Ilm-3 Gm	Ti-Mt-1 Gm	Ti-Mt-3 Gm	Ilm-1 Gm	Ti-Mt-1 Gm	Ti-Mt-2 Gm	Ti-Mt-3 Gm	Ilm-3 Gm	Ilm-2 Gm	Ilm-6 Gm	Ti-Mt-1 Gm	Ilm-2 Gm	Ilm-5 Gm
TiO_2	63·79	55·12	52·95	21·79	18·13	44·68	22·06	22·47	22·33	49·81	49·12	50·95	6·90	45·10	44·71
Al_2O_3	—	—	—	2·59	3·50	0·42	2·13	2·94	3·05	—	—	—	1·43	—	—
FeO_{Tot}	30·72	38·94	39·85	61·54	60·51	44·71	65·76	65·39	66·30	45·44	46·37	44·13	75·25	45·85	46·04
MnO	0·43	0·70	0·77	0·38	—	0·34	0·85	0·47	0·47	0·51	0·59	0·58	0·81	0·37	0·39
MgO	1·72	2·30	3·07	0·98	2·92	0·75	1·82	2·65	2·49	1·29	1·05	2·00	—	3·18	2·64
Cr_2O_3	—	—	—	—	1·16	—	—	—	—	—	—	—	0·43	—	—
V_2O_5	—	—	—	1·07	1·51	1·03	1·46	1·37	1·31	—	—	—	1·24	—	—
Total	96·66	97·06	96·64	88·35	87·73	91·93	94·08	95·29	95·95	97·05	97·13	97·66	86·06	94·5	93·78
Ulvöspinel				66·85	67·95		62·98	62·20	62·04				21·68		
Spinel				6·22	7·16		6·47	6·66	6·29				3·52		
Chromite				—	—		—	—	—				0·70		
Magnetite				26·92	24·89		30·55	31·14	31·66				74·10		

Rock type:	HT2-Bas									HT2-Pi					
Sample:	LAL3				LAL14					LAL6					
Mineral:	Ti-Mt-4 Gm	Ti-Mt-7 Gm	Ilm-1 Gm	Ilm-5 Gm	Ti-Mt-2 Gm	Ti-Mt-3 Gm	Ilm-2 Gm	Ilm-4 Gm	Ilm-5 Gm	Ti-Mt-4 Gm	Ti-Mt-6 Gm	Ti-Mt-1 Gm	Ilm-5 Gm	Ilm-1 Gm	Ilm-3 Gm
TiO_2	11·09	11·99	45·19	46·63	11·88	10·67	45·77	47·68	47·43	18·71	21·21	14·55	47·41	44·80	58·28
Al_2O_3	1·51	2·13	—	—	1·86	1·64	—	—	—	1·79	1·70	1·75	—	—	1·09
FeO_{Tot}	74·04	72·00	43·89	41·97	69·70	73·88	45·89	41·88	42·85	69·35	67·78	74·21	45·66	48·67	30·76
MnO	—	—	0·57	0·42	—	—	0·40	0·41	0·42	0·52	0·55	0·54	0·53	0·40	
MgO	0·98	1·51	3·01	3·26	1·56	1·28	2·36	3·94	3·56	3·09	3·19	1·73	3·30	1·21	3·86
Cr_2O_3	—	—	—	—	6·26	3·04	—	—	—	—	—	—	—	—	—
V_2O_5	0·95	0·75	—	—	0·90	0·99	—	—	—	0·84	—	0·77	—	—	—
Total	88·57	88·38	92·66	92·28	92·16	91·5	94·42	93·91	94·26	94·3	94·43	93·55	96·9	95·08	93·99
Ulvöspinel	34·06	35·09			34·63	31·33				52·83	55·89	41·70			
Spinel	3·91	—			4·24	3·76				3·97	4·42	3·93			
Chromite	—	—			—	4·69				—	—	—			
Magnetite	62·03	64·91			51·54	60·22				43·2	39·69	54·37			

Ti-Mt, titano-magnetite; Ilm, ilmenite. For the same sample, numbers refer to different crystals, letters to different analyses. Other abbreviations as in Tables 1–3.

in the groundmass of all magma types, and are extremely abundant in the HT2 lavas.

Northern Ethiopian mantle xenoliths

The mantle xenoliths included in the Quaternary alkaline lavas from the plateau area show a wide compositional range varying from spinel lherzolites to harzburgites and olivine-websterites. The dominant lherzolites (Table 7) are protogranular and generally lack modal evidence of metasomatic reaction. Their modal composition is in the following ranges: olivine 60–61%, orthopyroxene 22%, clinopyroxene 14–15%, spinel 3%.

Representative microprobe analyses of the main constituent minerals in the lherzolites are reported in Table 8.

Table 6: Representative analyses of feldspar and phlogopite from Northern Ethiopian CFBs

Rock type:	LT-Bas							HT1-Bas							HT2-Bas		
Sample:	ADG4			SIM7				LAL20							LAL1		
Mineral:	Pl-1 Gm	Pl-2 Gm	Pl-3 Gm	Pl-1 Gm	Pl-2 Gm	Pl-3 Gm	Pl-4 Gm	Pl-11 Gm	Pl-7 Gm	Pl-9 Gm	Pl-1 Gm	Pl-2 Gm	Pl-3 Gm	Pl-1 Gm	Pl-2 Gm	Pl-3 Gm	Pl-4 Gm
SiO_2	52·35	51·12	55·27	54·42	49·25	49·88	54·51	53·60	57·36	57·33	53·04	55·21	55·11	54·48	54·47	58·64	56·24
TiO_2	—	—	—	—	—	—	—	—	—	—	—	—	0·25	—	—	—	—
Al_2O_3	29·05	29·63	27·56	27·61	30·61	29·82	27·25	29·56	26·79	26·63	29·64	28·49	27·03	27·74	26·61	24·53	26·44
FeO_{Tot}	0·57	0·76	0·75	0·87	0·70	0·97	0·86	0·69	0·61	0·72	0·67	0·61	0·60	1·10	1·00	0·66	0·89
MnO	—	—	—	—	—	—	—	—	—	—	—	—	—	—	—	—	—
MgO	—	—	—	—	—	—	—	—	—	—	—	—	—	—	—	—	—
CaO	13·02	13·46	10·62	11·11	14·51	14·33	11·01	12·97	9·63	9·50	12·52	11·60	10·39	10·85	1-	7·51	9·27
Na_2O	4·43	4·08	5·79	5·01	3·17	3·22	5·35	4·58	6·47	6·41	4·46	5·40	5·77	5·19	5·55	7·21	6·07
K_2O	—	—	0·24	0·18	—	—	0·20	—	0·37	0·44	—	0·28	0·28	0·38	0·47	0·67	0·55
Total	99·41	99·05	100·24	99·21	98·24	98·21	99·19	101·40	101·23	101·03	100·34	101·60	99·43	99·75	98·10	99·22	99·46
an	62	65	50	54	72	71	53	61	44	44	61	53	49	52	49	35	44
ab	38	35	49	45	28	29	46	39	54	54	39	45	49	46	49	61	53
or	—	—	1	1	—	—	1	—	2	2	—	2	2	2	2	4	3

Rock type:	HT2-Bas													HT2-Pi		
Sample:	LAL3					LAL14								LAL6		
Mineral:	Pl-1 Gm	Pl-2 Gm	Pl-3 Gm	Pl-4 Gm	Pl-5 Gm	Pl-1 Gm	Pl-2 Gm	Af-2 Gm	Af-3 Gm	Af-4 Gm	Phlog-2 Gm	Phlog-4 Gm	Phlog-7 Gm	Pl-1 Gm	Pl-2 Gm	Af Gm
SiO_2	54·45	55·19	58·79	55·85	54·63	58·04	57·82	65·52	65·26	65·69	40·44	40·50	41·26	54·59	55·29	64·72
TiO_2	0·30	—	—	—	0·28	—	—	—	—	—	4·32	4·23	4·32	—	—	0·28
Al_2O_3	27·88	27·81	24·46	27·38	27·49	24·82	24·92	20·09	19·13	18·65	10·77	10·77	10·93	27·61	27·99	19·20
FeO_{Tot}	0·98	0·95	0·97	0·93	0·89	1·30	1·16	0·49	0·45	0·39	8·78	8·04	8·73	0·96	0·85	0·69
MnO	—	—	—	—	—	—	—	—	—	—	—	—	—	—	—	0·02
MgO	—	—	—	—	—	0·42	—	—	—	—	20·53	20·34	20·46	—	—	0·01
CaO	11·09	10·60	7·54	10·21	10·73	7·89	7·59	1·74	0·99	0·83	—	—	—	11·27	11·17	2·88
Na_2O	5·18	5·22	5·85	5·61	5·33	5·82	6·88	6·74	4·86	4·98	1·02	0·83	1·04	4·98	5·03	6·73
K_2O	0·52	0·45	1·91	0·55	0·50	0·94	0·77	6·13	9·10	9·32	8·57	8·68	8·72	0·42	0·47	5·22
Total	100·39	100·23	99·52	100·54	99·85	99·23	99·14	100·71	99·81	99·86	94·42	93·38	95·46	99·83	100·80	99·75
an	53	52	37	49	51	40	36	8	4	4				54	54	14
ab	44	46	52	48	46	54	59	58	43	43				44	44	57
or	3	2	11	3	3	6	5	34	53	53				2	2	29

an, anorthite; ab, albite; or, orthoclase. For the same sample, numbers refer to different crystals, letters to different analyses. Other abbreviations as in Tables 1–3.

Mineral compositions are rather homogeneous with olivine $Fo_{88–90}$, orthopyroxene $En_{88–90}$, diopsidic clinopyroxene, and brown spinel with mg-number 0·77–0·80 and cr-number 0·08–0·12.

Thermobarometric estimates according to Brey & Köhler (1990) and Köhler & Brey (1990) give nominal equilibration temperatures between 930 and 1050°C and a pressure range of 9–12·5 kbar, which is in agreement with the spinel peridotite stability conditions previously determined for Ethiopian mantle xenoliths (Conticelli *et al.*, 1999). Therefore, they can be considered as representative of the local subcontinental lithospheric mantle.

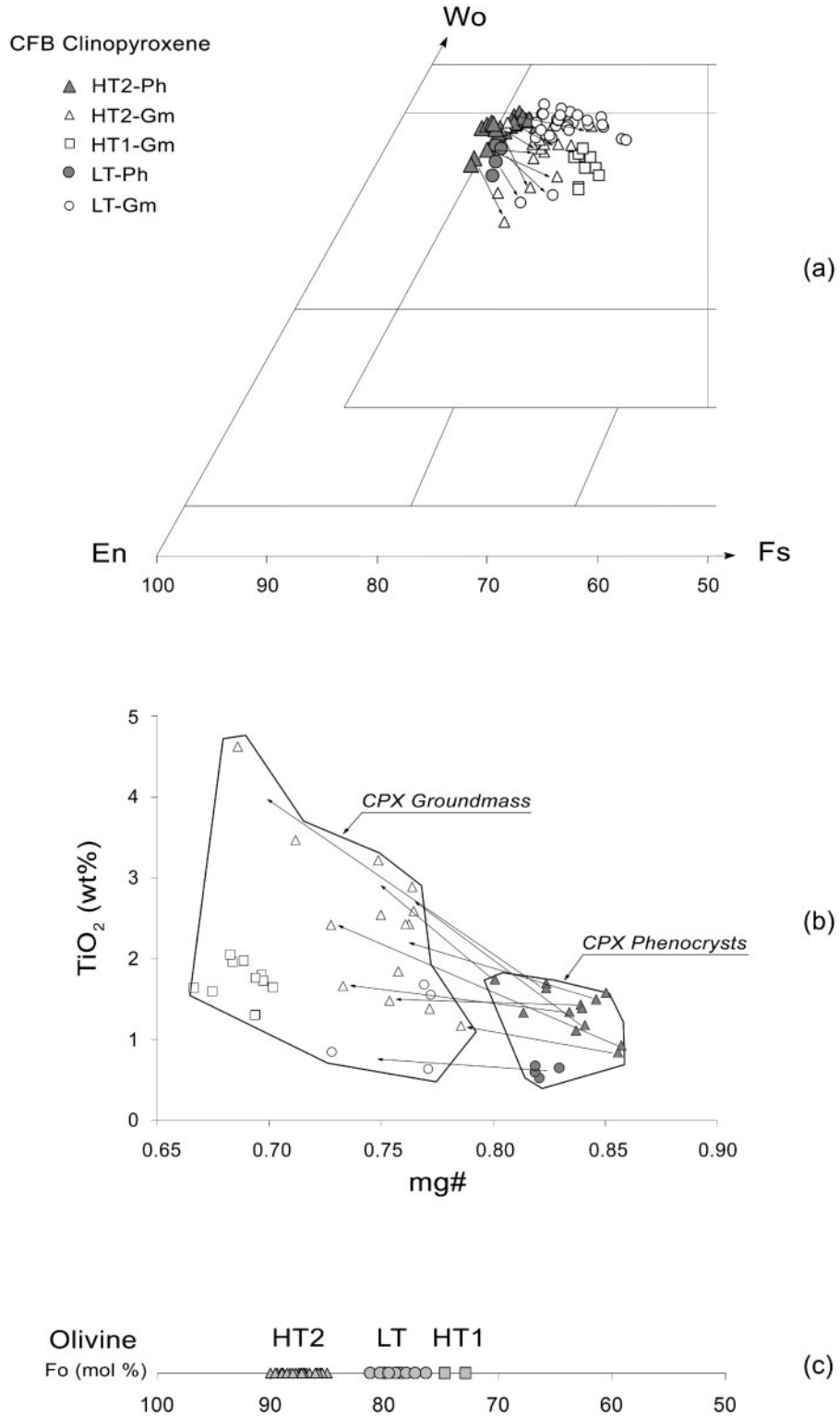

Fig. 6. (a) Pyroxene quadrilateral (mol%) and (b) TiO_2 vs mg-number for clinopyroxenes from the Northern Ethiopian CFBs. Lines join phenocryst (Ph) and groundmass (Gm) crystals. mg-number = $Mg/(Mg + Fe^2)$. (c) Compositional range of olivine phenocrysts from the Northern Ethiopian CFBs (including analyses from Pik *et al.*, 1998). En, enstatite; Fs, ferrosilite; Wo, wollastonite; Fo, forsterite. Other abbreviations as in Fig. 1.

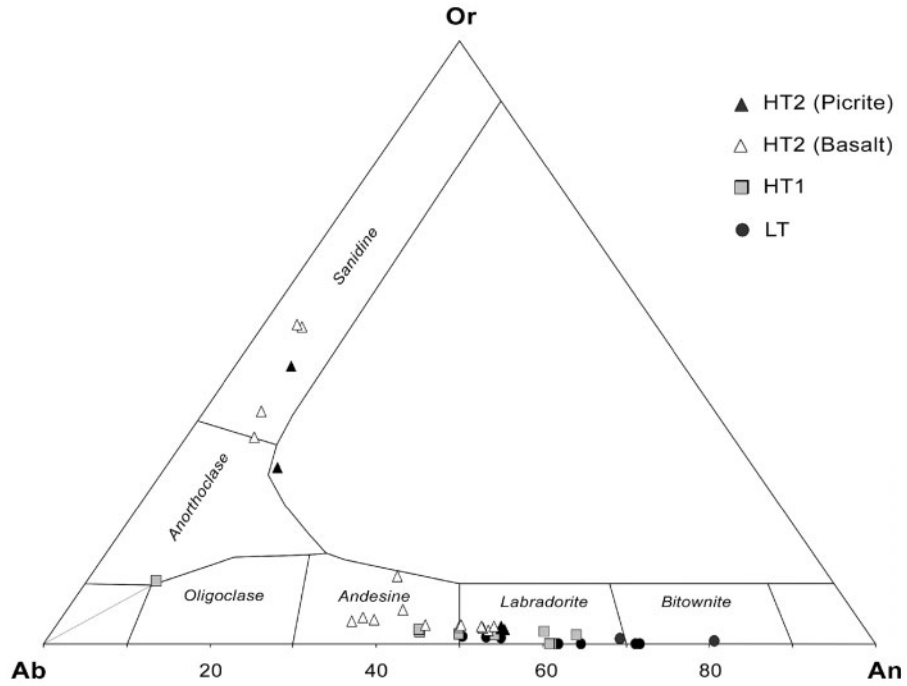

Fig. 7. Or–Ab–An (mol%) ternary diagram for feldspars from the Northern Ethiopian CFBs (including analyses from Pik *et al.*, 1998). Or, orthoclase; Ab, albite; An, anorthite. Other abbreviations as in Fig. 1.

Spinel lherzolite xenoliths from a single Miocene alkali basalt flow in the Simien Mountains section (Roger *et al.*, 1997; Ayalew *et al.*, 2009) show textural and mineralogical features, as well as equilibration temperatures (900–1100°C), closely comparable with those of xenoliths included in the Quaternary volcanic rocks.

TRACE ELEMENT GEOCHEMISTRY

The trace element characteristics of Northern Ethiopian LT, HT1 and HT2 CFBs are illustrated in mantle-normalized diagrams in Fig. 8. Their chondrite-normalized REE patterns show light REE (LREE) enrichment gradually increasing from LT (La_N/Yb_N 1·2–3·3) to HT1 tholeiites (La_N/Yb_N 6·9–7·5) and to ultra-titaniferous HT2 transitional basalts and picrites (La_N/Yb_N 11·3–17·5). The extended Primordial Mantle (PM)-normalized incompatible element patterns of LT and HT1 reveal a general similarity to other CFB provinces (Macdougall, 1988; Piccirillo & Melfi, 1988; Ellam & Cox, 1991; Gallagher & Hawkesworth, 1992; Melluso *et al.*, 1995; Peate, 1997). On the other hand, the HT2 lavas resemble transitional or alkaline ocean island basalts (OIB) from enriched mantle sources in within-plate settings (Weaver, 1991; Sun & McDonough, 1995; Hofmann, 1997).

LT basalts have a relatively low Nb/La ratio, which, in principle, may be attributed to crustal contamination (Pik *et al.*, 1998). The influence of this process has been demonstrated to some extent on the basis of isotopic data for some Ethiopian (Pik *et al.*, 1999) and Yemen (Baker *et al.*, 2000) CFBs. However, the systematic increase of the Nb/La ratio from LT to HT2, parallel to the trend of incompatible element enrichment, suggests that this variation has to be mostly attributed to an increasing metasomatic enrichment of their mantle sources. Similar conclusions have been reached by Kieffer *et al.* (2004), who have confirmed significant trace element differences between the LT and HT parental magmas within the Ethiopian CFBs, after removing the possible effects of fractional crystallization and crustal contamination.

Additional evidence for original differences between the LT and HT magmas from the Northern Ethiopian plateau is provided by their clinopyroxene trace element patterns (Table 9, Fig. 9). Clinopyroxene from LT basalts is characterized by LREE depletion (La_N/Yb_N down to 0·13) typical of tholeiitic basic magmas from both oceanic and continental settings, precluding the occurrence of significant crustal contamination. On the other hand, clinopyroxene phenocrysts from the HT2 basalts and picrites reveal distinctive convex-upward patterns with La_N/Yb_N 1·0–3·6 and Sm_N/Yb_N 3·3–7·3, resembling those commonly recorded in alkaline magmas (Jeffries *et al.*, 1995), which is in agreement with the transitional affinity of the respective bulk-rocks. The significant heavy REE (HREE) fractionation (Tb_N/Yb_N 2·7–4·3 and 2·7–6·0

Table 7: Bulk-rock major and trace element analyses of lherzolite mantle xenoliths from Northern Ethiopia and their basanitic host lavas

Rock type:	Lherzolite mantle xenoliths				Host lavas	
Locality:	Injibara		Dedessa		Injibara	Dedessa
Longitude:	37°02′09″		36°10′01″		37°02′09″	36°10′01″
Latitude:	10°50′27″		09°01′34″		10°50′27″	09°01′34″
Sample:	GOJ26	GOJ40A	WOL8	WOL39	GOJ 32	WOL51B
SiO_2	44·29	44·01	44·59	46·68	47·57	44·13
TiO_2	0·14	0·17	0·14	0·18	1·62	2·93
Al_2O_3	3·49	3·82	2·46	3·10	17·90	14·37
$Fe_2O_{3\ Tot}$	8·26	7·76	8·54	8·10	10·89	11·93
MnO	0·13	0·13	0·14	0·12	0·21	0·19
MgO	40·27	40·12	40·10	36·95	4·98	8·15
CaO	2·68	3·36	2·85	2·79	7·66	9·58
Na_2O	0·28	0·42	0·28	0·36	5·97	4·05
K_2O	0·00	0·01	0·04	0·18	2·22	1·92
P_2O_5	0·02	0·01	0·02	0·03	0·54	0·70
LOI	0·44	0·19	0·86	1·49	0·45	2·06
mg-no.	0·92	0·91	0·90	0·90	0·51	0·61
Ni (ppm)	1961	1878	2034	1961	60	149
Co	106	103	119	111	25	34
Cr	2244	2102	1026	2078	112	256
V	74	85	65	71	163	257
Sc	17	17	17	17	15	31
Sr	14	17	12	35	788	873
Ba	nd	nd	nd	nd	925	620
Zr	nd	nd	nd	nd	167	241
Hf	0·21	0·28	0·27	0·28	3·79	5·52
Nb	0·35	0·46	0·91	1·37	110	76·5
Ta	0·06	0·06	0·09	0·11	6·50	4·28
Th	0·05	0·09	0·10	0·15	11·2	6·29
U	0·03	0·10	0·03	0·06	2·33	1·57
Y	3·05	3·88	3·40	3·35	28·8	28·6
La	0·36	0·54	0·85	1·25	69·8	54·5
Ce	0·81	1·32	1·90	2·66	116	100
Pr	0·12	0·19	0·25	0·33	12·6	11·1
Nd	0·70	1·08	1·35	1·64	46·0	44·6
Sm	0·23	0·34	0·39	0·40	6·89	7·81
Eu	0·09	0·13	0·14	0·14	2·34	2·52
Gd	0·29	0·39	0·41	0·43	6·78	7·12
Tb	0·08	0·10	0·11	0·09	0·90	1·05
Dy	0·51	0·68	0·66	0·60	5·00	5·54
Ho	0·13	0·16	0·16	0·14	0·86	0·99
Er	0·37	0·45	0·46	0·39	2·66	2·75
Tm	0·06	0·07	0·08	0·06	0·40	0·39
Yb	0·40	0·46	0·46	0·39	2·59	2·42
Lu	0·05	0·06	0·07	0·06	0·36	0·32

mg-number = mol $MgO/(MgO + FeO_{tot})$. Other abbreviations as in Table 1.

in basalts and picrites, respectively) in these clinopyroxenes may support the idea that initial melting of the mantle source of the HT magmas occurred in the presence of residual garnet (Hellebrand & Snow, 2003).

PETROGENETIC MODELLING

In any petrogenetic model dealing with the origin of primary basaltic melts and their geodynamic significance, the P–T conditions of melting, the source composition and the degree of melting (F) are of primary consideration. Moreover, the presence of mantle xenoliths in the studied area can provide further petrogenetic constraints, as they represent direct evidence of the underlying lithospheric mantle. In the following discussion quantitative modelling based on the major and trace element composition of both Northern Ethiopian CFBs and mantle xenoliths is carried out to constrain the P–T–X conditions of the mantle melting region from which the magmas were generated.

Major elements

Different approaches based on major elements were used to develop a comprehensive petrogenetic model for the least differentiated CFBs from the three groups, which all include (with the exception of HT1) samples with mg-number between 0·68 and 0·72; that is, in equilibrium with mantle sources containing olivine $Fo_{\geq 88}$ (Herzberg & O'Hara, 2002; Green & Falloon, 2005). It should be noted that most of the Northern Ethiopian CFBs have lower mg-number and only a few HT2 picrites (non olivine-cumulative) reach the threshold of mg-number 0·72 that was considered by Niu & O'Hara (2008) as the required value for true primary magmas. However, the relatively low mg-number values of CFBs from Northern Ethiopia are, at least in part, related to the distinctive Fe enrichment that appears to be a primary feature of these magmas. Therefore, model calculations, reported below, have been carried out on a large dataset (also including analyses by Pik *et al.*, 1998) for basalts with MgO $\geq$6%, which represents the compositional limit for olivine to be considered the main phase controlling the liquid line of descent (Herzberg & Asimow, 2008).

The Niu & Batiza (1991) empirical model was first applied to estimate the degree of melting (F), and the initial (P_0) and final (P_f) melting pressure of the Northern Ethiopian basalts, assuming that they formed along a melting column from mantle sources under decompression conditions. Basalt compositions out of the range of the experimental data on which the model was based were discarded and analyses with MgO < 8% were normalized to MgO = 8% by adding an appropriate amount of olivine Fo_{87}, which represents the most magnesian phenocryst composition observed in the Northern Ethiopian basalts. These data were integrated with the pressure (P_A) and

Table 8: Representative mineral analyses of lherzolite mantle xenoliths from Northern Ethiopia

Mineral:	Olivine					Orthopyroxene					
Sample:	GOJ26-1d rim	GOJ26-1e core	GOJ40-1b rim	GOJ40-2c core	WOL8-2a core	GOJ26-1c rim	GOJ26-3a core	GOJ40A-1c core	GOJ40A-2d rim	WOL8-1a core	WOL8-2c core
SiO_2	41·88	41·61	41·74	41·79	41·11	56·59	56·60	56·32	56·67	54·73	55·49
TiO_2	—	—	0·02	—	0·10	0·11	0·08	0·14	0·09	0·17	0·17
Al_2O_3	0·02	0·03	0·03	0·03	0·04	3·88	3·79	4·12	4·19	5·06	4·78
FeO_{Tot}	10·21	10·47	10·32	10·48	10·93	6·55	6·60	6·86	6·60	7·36	7·19
MnO	0·19	0·14	0·12	0·10	0·06	0·14	0·18	0·06	0·14	0·11	0·17
MgO	48·29	48·94	48·26	48·09	47·34	33·05	32·72	32·21	32·87	31·27	31·70
CaO	0·09	0·04	0·04	0·10	0·09	0·52	0·51	0·63	0·58	0·80	0·73
Na_2O	—	0·04	—	0·01	0·02	0·09	0·09	0·09	0·16	0·16	0·15
K_2O	0·01	—	0·02	0·01	0·01	—	0·02	—	—	0·01	—
Cr_2O_3	0·04	—	0·05	—	0·02	0·23	0·23	0·34	0·27	0·16	0·19
NiO	0·39	0·46	0·32	0·27	0·39	0·16	0·12	0·09	0·13	0·11	—
Total	101·13	101·74	100·92	100·87	100·10	101·09	101·01	101·07	101·12	101·17	101·03
mg-no.	0·89	0·89	0·89	0·89	0·88	0·90	0·89	0·89	0·90	0·88	0·89

Mineral:	Clinopyroxene						Spinel				
Sample:	GOJ26-3c core	GOJ26-4a core	GOJ40A-1a core	GOJ40A-2b rim	WOL8-1e core	WOL8-1b rim	GOJ26-1a core	GOJ40A-1e rim	GOJ40A-3a core	WOL20B-1L core	WOL20B-2C core
SiO_2	52·74	52·90	52·60	52·93	51·51	55·69	0·30	0·47	0·32	0·02	0·03
TiO_2	0·61	0·64	0·66	0·65	0·62	0·17	0·10	0·08	0·07	0·08	0·05
Al_2O_3	7·01	7·16	7·06	6·80	5·49	0·84	59·61	59·46	60·80	57·67	56·88
FeO_{Tot}	2·59	2·53	2·73	2·87	3·54	3·25	10·27	9·55	10·55	9·93	9·45
MnO	0·05	0·06	0·04	0·07	0·10	0·16	0·04	0·12	0·05	0·15	0·12
MgO	14·10	14·01	14·70	14·48	15·57	19·17	19·96	20·34	19·97	21·14	21·00
CaO	20·55	20·22	20·77	20·57	21·99	20·55	—	0·02	0·01	—	0·01
Na_2O	1·88	2·05	1·69	1·60	0·59	0·46	0·03	0·02	0·05	—	—
K_2O	—	0·02	—	—	0·02	0·11	0·02	0·02	0·03	—	0·02
Cr_2O_3	0·83	0·95	0·65	0·70	0·65	0·53	8·88	9·24	7·78	10·92	11·17
NiO	0·03	0·07	—	0·16	0·09	0·14	0·52	0·44	0·45	0·30	0·37
Total	100·37	100·56	100·89	100·84	100·17	101·06	99·22	99·77	100·06	100·22	99·11
mg-no.	0·91	0·91	0·91	0·90	0·89	0·88	0·78	0·79	0·77	0·81	0·82
cr-no.							0·09	0·09	0·08	0·11	0·12

Abbreviations as in Table 3. For the same sample, numbers refer to different crystals, letters to different analyses.

temperature (T) of melt segregation calculated using the algorithm of Albarède (1992). For picrites, which fall outside the composition range investigated by Niu & Batiza (1991), only the Albarède thermobarometric approach was used, and $F = 25$–30% was assumed in accordance with experimental petrology data (Green & Falloon, 2005, and references therein).

Results are reported in the P–T petrogenetic grid of Fig. 10. Temperatures of basalt segregation range from 1400°C for HT to 1200°C for LT. In picrites, higher segregation temperatures (up to 1500°C) are recorded in accordance with both the exceedingly high Ni content (1100–650 ppm in bulk-rocks) and the high Cr content of their olivine phenocrysts (up to 1000 ppm), which conform with plume-derived superheated magmas (Campbell, 2001).

Further temperature estimates for picrites have been obtained using olivine–liquid thermometers according to

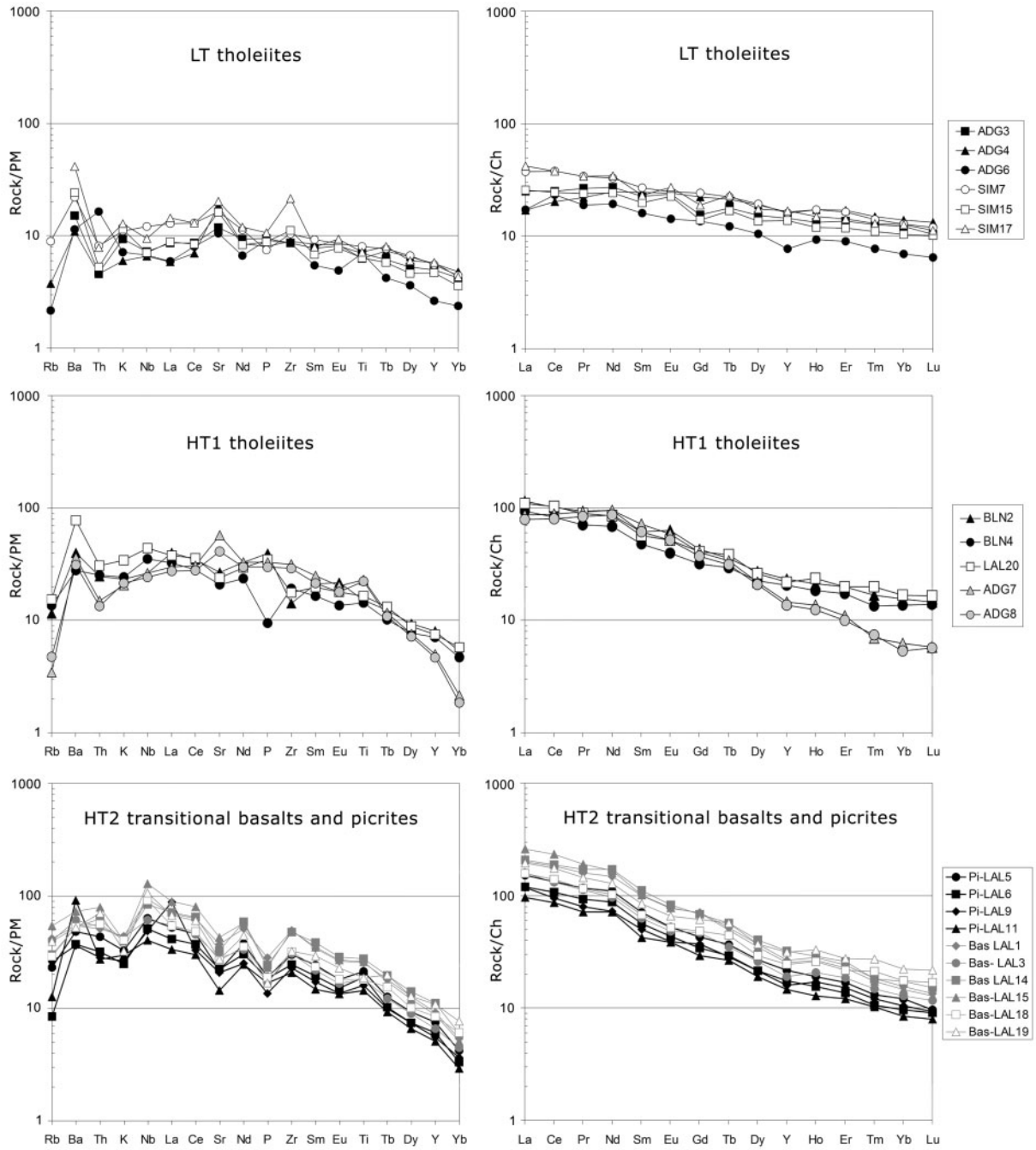

Fig. 8. Primordial Mantle (PM)-normalized incompatible element and chondrite (Ch)-normalized REE patterns for CFBs from the Northern Ethiopian plateau. Normalizing factors after Sun & McDonough (1989) and McDonough & Sun (1995), respectively. Abbreviations as in Fig. 1.

Ford *et al.* (1983) and Herzberg & O'Hara (2002), giving temperatures of ~1400°C (in equilibrium with Fo_{90} olivine) and 1360–1365°C (in equilibrium with Fo_{88} olivine) for samples LAL6 and LAL9, respectively. As expected, these olivine liquidus temperatures are systematically lower (by some 50–100°C) than those calculated for magma segregation from the mantle sources. This allows us to conclude that, even considering the possible H_2O effect in lowering the liquidus temperature (Falloon *et al.*, 2007), the generation conditions of the hottest (picritic) magmas has to be ≥1350°C.

These results emphasize that the zonal arrangement of Northern Ethiopian CFBs from LT in the west to HT2 in the east broadly corresponds to a parallel increase in

Table 9: LA–ICP–MS trace element analyses of clinopyroxene from representative Northern Ethiopian CFBs

Rock type:	LT-Bas							HT2-Bas				HT2-Pi			
Sample:	ADG4					ADG3		LAL14				LAL5	LAL9		
	Cpx-2a	Cpx-2b	Cpx-5b	Cpx-5c	Cpx-5d	Cpx-1a	Cpx-1b	Cpx-2a	Cpx-2b	Cpx-3a	Cpx-3b	Cpx-1a	Cpx-2b	Cpx-2c	Cpx-4a
Sr (ppm)	23·4	26·4	29·7	28·0	27·1	31·0	28·2	110	111	124	116	49·9	37·4	39·7	45·0
Y	20·9	20·1	27·4	24·3	21·7	28·9	28·4	12·0	12·9	19·9	18·8	6·62	5·62	6·11	7·21
Zr	22·3	29·1	40·5	38·6	31·8	53·4	39·9	36·6	36·1	52·4	48·3	11·8	7·53	8·17	13·0
Hf	0·91	2·25	1·89	2·13	1·28	2·06	1·41	1·85	1·70	2·09	2·05	0·43	0·43	0·22	0·66
Nb	<0·02	0·07	<0·02	0·10	0·08	0·07	0·02	0·21	0·16	0·18	0·21	0·05	0·03	0·03	0·05
Ta	<0·01	0·01	<0·01	<0·01	<0·01	0·04	<0·01	0·02	0·01	0·01	0·02	<0·01	<0·01	<0·01	0·01
La	0·41	0·56	0·68	0·68	0·66	1·42	1·20	2·75	2·94	4·46	3·82	1·29	0·68	0·63	0·94
Ce	2·61	3·01	3·74	3·40	3·15	5·85	5·22	13·1	13·8	19·1	17·8	4·84	2·56	2·68	3·74
Pr	0·76	1·01	0·95	0·91	0·85	1·18	1·22	2·9	2·5	3·62	3·43	0·98	0·48	0·62	0·70
Nd	5·13	6·74	6·97	7·20	6·05	10·1	9·89	17·0	15·7	24·3	21·9	5·61	3·52	3·76	4·89
Sm	3·57	3·26	2·90	3·33	2·60	4·17	3·98	5·76	5·63	7·87	7·24	1·76	1·13	1·4	2·01
Eu	0·96	1·17	1·14	1·03	1·08	1·27	1·23	1·32	1·80	2·61	2·35	0·66	0·44	0·41	0·61
Gd	3·55	3·64	5·00	3·98	3·53	5·47	4·69	4·98	4·60	7·58	6·29	1·53	1·61	1·56	1·65
Tb	0·60	0·55	0·94	0·85	0·70	0·95	0·80	0·52	0·66	1·05	0·87	0·26	0·30	0·22	0·36
Dy	3·96	3·56	5·79	5·34	3·92	4·72	5·37	3·04	3·56	5·06	4·02	1·61	1·33	1·28	1·71
Ho	0·78	0·87	1·23	0·93	0·72	1·07	1·20	0·49	0·56	0·91	0·67	0·30	0·23	0·23	0·33
Er	1·94	2·13	2·88	2·31	1·98	3·13	3·18	1·08	1·14	1·78	1·53	0·54	0·56	0·48	0·72
Tm	0·31	0·31	0·36	0·32	0·30	0·35	0·45	0·14	0·11	0·22	0·19	0·07	0·07	0·1	0·08
Yb	2·06	1·96	2·01	2·04	1·87	2·20	3·48	0·86	0·68	1·39	1·35	0·41	0·22	0·37	0·59
Lu	0·17	0·31	0·31	0·33	0·27	0·31	0·39	0·06	0·10	0·15	0·19	0·07	0·05	0·06	0·07
Th	<0·01	0·02	0·01	0·02	0·02	0·02	0·01	0·04	0·02	0·01	0·03	<0·01	0·02	<0·01	0·01
U	<0·01	0·02	<0·01	<0·01	<0·01	<0·01	<0·01	<0·01	0·01	<0·01	0·01	<0·01	<0·01	<0·01	<0·01

Abbreviations as in Tables 1–3. For the same sample, numbers refer to different crystals, letters to different analyses.

magma temperature. Moreover, the temperature difference between the hottest Ethiopian CFBs and the ambient mantle, represented by mantle xenoliths from the area, is at least $\geq 300^{\circ}$C, which is compatible with the thermal anomaly induced by a deep mantle plume (Farnetani & Richards, 1994; Campbell, 2007). The geothermal regime seems to vary from nearly adiabatic (potential temperature $T_p = 1430^{\circ}$C), with generation of the hottest picritic magmas over a pressure interval of 1·6–3·0 GPa, to non-adiabatic, where LT magmas were formed. This implies that the mantle region that underwent partial melting had its deepest and hottest part centred in the east, close to the Afar triple junction, where a deep plume has been recorded by seismic tomography (Davaille *et al.*, 2005). This is fully consistent with the petrological model proposed by Herzberg & O'Hara (2002) for plume-associated picritic magmas.

The interpolation of the P_0 values of the initial melts for the LT and HT magmas defines two distinct near-solidus mantle arrays located between the dry and the volatile-bearing peridotite solidi (Fig. 10). The HT initial melting array is closer to the H–O–C-bearing lherzolite solidus, suggesting a more volatile-enriched nature for their mantle sources, as also indicated by the significant presence of hydrous phases in some HT basalts.

Major element mass-balance calculations between the basalts and the lherzolite xenoliths (Tables 1 and 7) were also carried out to further constrain the composition of the mantle sources, using F estimates obtained from the model above. The modal mineral composition of the mantle sources, as well as the melting proportions, were defined by iterative least-squares calculations based on the major element compositions of the constituent minerals (Table 8) plus additional mantle phases such as amphibole–phlogopite, garnet and ilmenite generally not present in the studied lherzolite xenoliths, but required by computation (see Table A1 in the Appendix). A summary of the modelling results is given in Table 10, which relates each

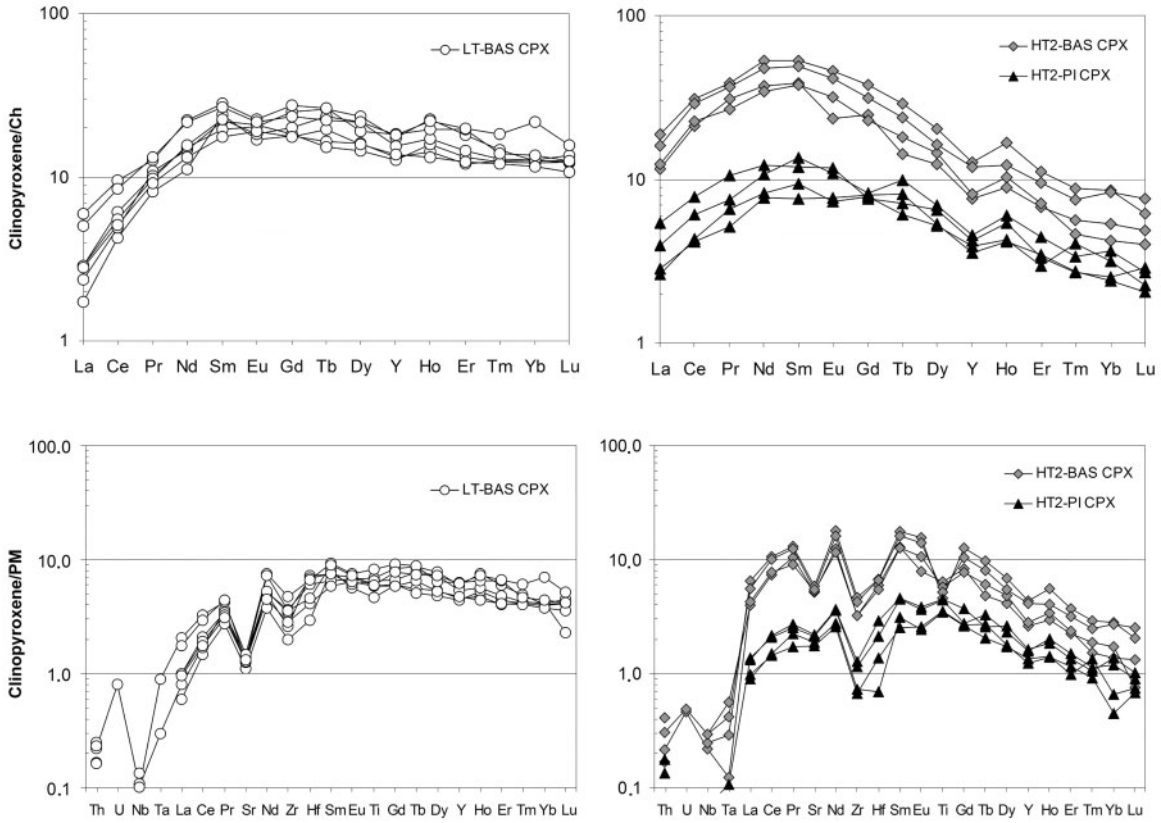

Fig. 9. Primordial Mantle (PM)-normalized incompatible element and chondrite (Ch)-normalized REE patterns of clinopyroxenes from representative Northern Ethiopian CFBs. Normalizing factors after Sun & McDonough (1989) and McDonough & Sun (1995), respectively. Abbreviations as in Fig. 1.

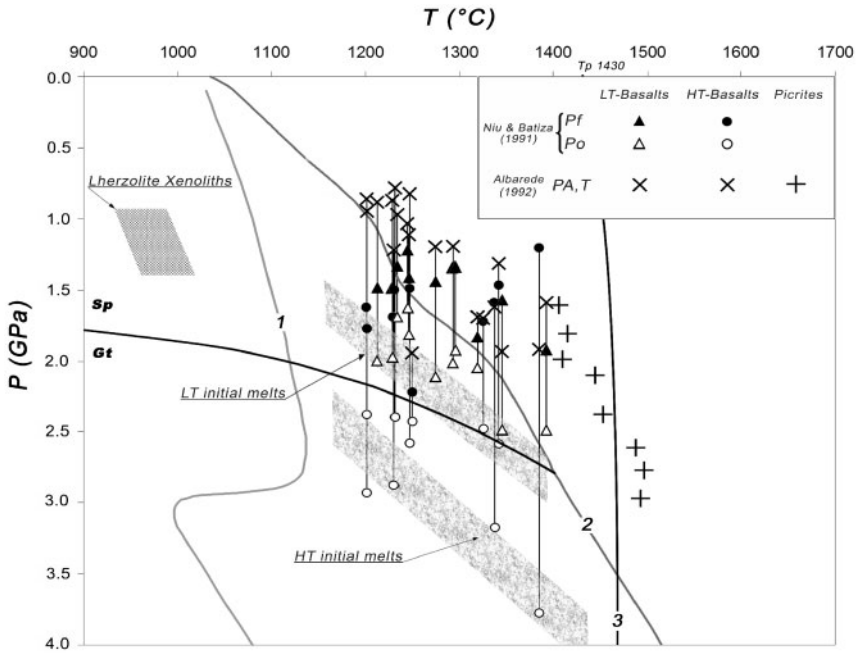

Fig. 10. Pressure (P)–temperature (T) petrogenetic grid depicting the melting conditions of Northern Ethiopian CFBs based on the model proposed by Niu & Batiza (1991) (P_0 and P_f are initial and final pressures of melt formation) and Albarède (1992) (P_A and T are pressure and temperature of melt segregation). Results from this study and Pik *et al.* (1998). Volatile (H–O–C)-bearing (1) and dry (2) lherzolite solidi, spinel (sp) and garnet (gt) stability fields, and adiabat (3) for mantle potential temperature T_p 1430°C are after Green & Falloon (2005). Shaded fields refer to the P–T equilibration conditions of lherzolite mantle xenoliths from Northern Ethiopia (this work and Conticelli *et al.*, 1999), HT and LT initial melts. (See text for further explanation.)

*Table 10: Calculated source modes, melting proportions, ranges of melting degrees (*F*%), P (GPa) and T (°C) conditions for LT basalts and HT basalts and picrites from the Northern Ethiopian CFBs*

Magma type, mineral	Source mode	Melting proportion	*F* (%) range	*P* (GPa) range	*T* (°C) range
LT basalt	$S_{LT\ bas}$	(*F* = 15%)	14–20	1·3–2·0	1200–1350
ol	64	−39			
opx	19	56			
cpx	8	13			
sp	2	5			
amph*	7	65			
HT basalt	$S_{HT1\ bas}$	(*F* = 20%)	15–25	1·4–2·2	1200–1400
ol	63	−10			
opx	11	14			
cpx	10	13			
gt	4	10			
amph*	10	64			
ph*	2	9			
HT picrite	$S_{HT2\ picr}$	(*F* = 30%)	25–30	1·6–3·0	1400–1500
ol	59	19			
opx	14	8			
cpx	11	28			
gt	4	2			
amph*	8	31			
ph*	2	7			
ilm*	2	5			

Least-squares mass-balance calculations on representative lava samples for the *F* values indicated in parentheses. ol, olivine; opx, orthopyroxene; cpx, clinopyroxene; sp, spinel; gt, garnet; amph, amphibole; ph, phlogopite; ilm, ilmenite. *Other mineral assemblage with equivalent chemical budget.

magma-type with the source mineralogy, melting proportions and degree, and the *P*–*T* conditions of melting. This indicates the following features.

(1) Chemical components corresponding to amphibole ± phlogopite are always required in the magma source, varying from 7% for LT tholeiites to 10–12% for HT basalts and picrites, and are the predominant melting phases. These phases, or another chemically equivalent mineral assemblage stable at the relevant *P*–*T* conditions, are considered to be related to metasomatizing agents interacting with the original mantle parageneses, and confirm the hydrated nature of the mantle solidus hypothesized in Fig. 10.

(2) Titanium-rich minerals (e.g. ilmenite, rutile, armalcolite) are additional metasomatic phases required in the mantle sources of the ultra-titaniferous (HT2) magmas.

(3) The presence of negative olivine in the melting proportions of the subalkaline melts, although decreasing from LT to HT1 tholeiites, reflects a significant incongruent melting of orthopyroxene in the source of the tholeiitic magmas (Beccaluva *et al.*, 1998).

(4) The significant presence of garnet required in both the mantle source and the melting proportions of the HT magmas confirms P_0 estimates of their initial melting conditions in the garnet lherzolite stability field (Fig. 10).

Incompatible elements

Further petrogenetic constraints are provided by the distribution of those incompatible trace elements that are widely recognized as indicators of OIB mantle sources in hotspot or plume regions. To evaluate quantitatively the incompatible element distribution in the magma sources, batch melting modelling was carried out based on the basalt compositions, using the melting parameters defined in the previous section. Results show that to generate the entire range of Ethiopian CFB magmas, from LT to HT, the calculated mantle sources ($S_{LT\ bas}$, $S_{HT1\ bas}$, $S_{HT2\ picr}$; Fig. 11) should be of the order of 2–15 times richer in incompatible elements with respect to those of the most fertile Northern Ethiopian mantle xenoliths. Significantly, these source compositions satisfactorily match those (S_1, S_2, S_3; Fig. 11) resulting from lherzolite xenoliths GOJ26 and GOJ40A with the addition of an amount of metasomatic amphibole plus Ti phases approaching that required by the major element mass-balance calculations (Table 10). The lherzolite xenoliths have flat mantle-normalized trace element patterns (0·7–1·0 × PM), showing little sign of incompatible element enrichment, in contrast to other xenolith occurrences in southern Ethiopia (Bedini *et al.*, 1997) and along the Saharan Belt (Hoggar, Algeria, Beccaluva *et al.*, 2007*a*; Gharyan, Libya, Beccaluva *et al.*, 2008).

The consistency of the major and trace element modelling suggests that the Northern Ethiopian CFBs were generated from lherzolite mantle sources variably metasomatized by alkali–silicate hydrous melts enriched in high field strength elements (HFSE; e.g. Ti, Nb, Zr), low field strength elements (LFSE; e.g. Ba and Th), and LREE. These metasomatizing agents show compositional similarities to those recorded in mantle xenoliths from the Kerguelen Islands, where both amphibole and Ti-rich metasomatic phases (including rutile, ilmenite and armalcolite) have been reported (Grégoire *et al.*, 2000).

The interpretation of this metasomatic enrichment is not straightforward, being related either to a contribution from the Earth's metallic core (Humayun *et al.*, 2004) or to the involvement of eclogitic materials recycled in the mantle (Sobolev *et al.*, 2007). However, the distinctive Ti

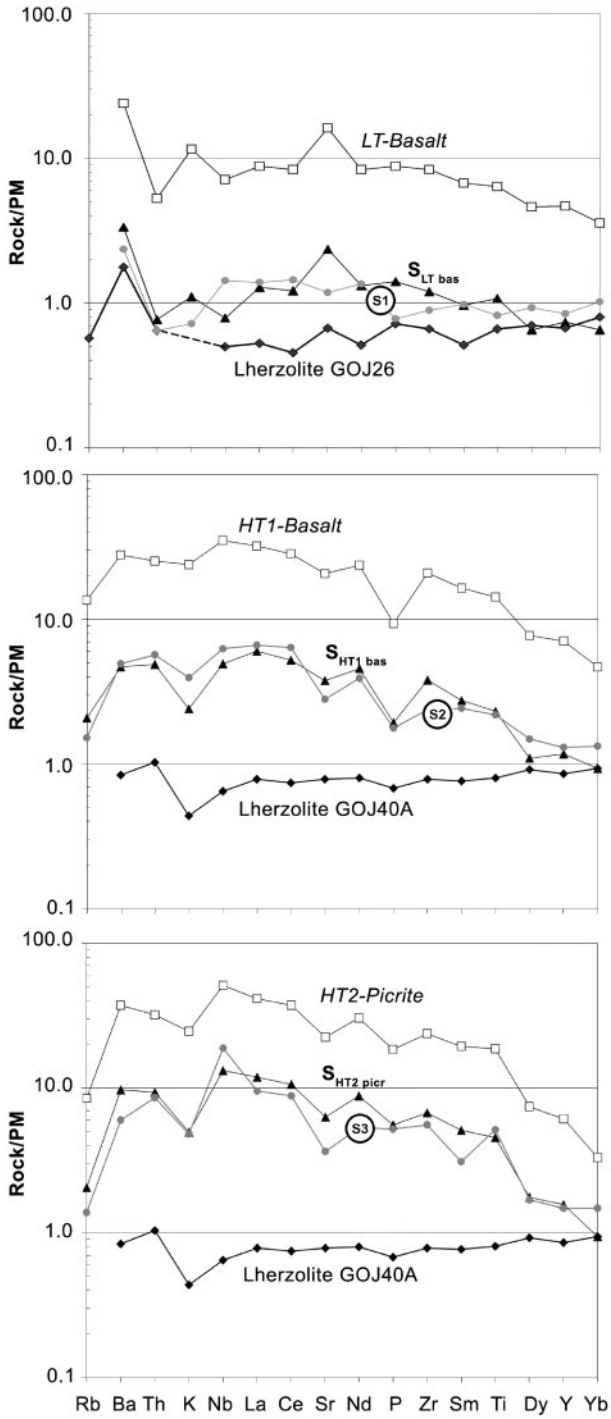

Fig. 11. Primitive Mantle (PM)-normalized (Sun & McDonough, 1989) incompatible element patterns of Northern Ethiopian LT and HT magmas and their inferred mantle sources. $S_{LT\ bas}$, $S_{HT1\ bas}$ and $S_{HT2\ picr}$ refer to source compositions calculated by batch melting for LT basalt SIM15, HT1 basalt BLN4 and HT2 picrite LAL6, using partition coefficients (K_d) from the GERM website (http://earthref.org/GERM) and melting parameters as defined in Table 10. These theoretical compositions favourably compare with those of Ethiopian mantle xenoliths GOJ26 and GOJ40A (Table 1) with the addition of appropriate metasomatic phases: S_1 = lherzolite GOJ26 (ol 61, opx 22, cpx 14, sp 3) + 3% amphibole (from Zabargad lherzolites; Brooker *et al.*, 2004); S_2 = lherzolite GOJ40A (ol 60, opx 22, cpx 15, sp 3) + 9% amphibole (from Kerguelen mantle xenoliths; Moine *et al.*, 2001); S_3 = lherzolite GOJ40A + 12% amphibole and 1% ilmenite (from Kerguelen mantle xenoliths; Grégoire *et al.*, 2000; Moine *et al.*, 2001).

enrichment observed in the Northern Ethiopian CFBs implies that the metasomatizing agents were enriched in this element, favouring an origin from mantle sources that included Ti-rich eclogitic materials. These materials most probably result from the recycling of Ti-rich mid-ocean ridge basalt (MORB) protoliths in the mantle via ancient subduction.

The origin of the volatile components in the metasomatizing agents is a matter of considerable debate. The helium isotopic composition of Ethiopian CFBs shows *Ra* up to 20 for some High-Ti magmas, suggesting an origin from the undegassed lower mantle (Pik *et al.*, 2006) or even from the D' layer at the core–mantle boundary (Tolstikhin & Hofmann, 2005). Analogous considerations are valid for the relatively high H_2O contents in the HT magmas. Studies on deep mantle components have in fact shown that nominally anhydrous minerals (NAM) such as olivine and orthopyroxene may actually contain a significant amount of water, whose origin could ultimately be related to primordial hydrogen residing in the Earth's core and interacting with lower mantle silicate parageneses (Williams & Hemley, 2001). Recent experimental results show that water solubility in orthopyroxene has a minimum in the asthenosphere (i.e. the low-velocity zone; Mierdel *et al.*, 2007), where excess water may further enrich the rising metasomatic agents, ultimately leading to hydrous mineral parageneses in the lower lithosphere and at the asthenosphere–lithosphere transition.

From the above it is evident that the inferred metasomatic agents could have integrated various mantle geochemical components with different provenance and mobility. These components probably pooled by scavenging and mixing of heterogeneous mantle materials during the ascent of the plume (Farnetani *et al.*, 2002).

CONCLUSIONS AND IMPLICATIONS FOR THE AFAR MANTLE PLUME

The spatial distribution of the various magma types, together with their petrogenetic P–T–X constraints, are used to define the shape, size and location of the melting region in the underlying mantle where the magmas were generated. Our results suggest an onion-like melting region (Fig. 12), most probably representing the head of an impinging deep mantle plume that induced a dramatic thermal anomaly, lithospheric bulging or faulting, and the

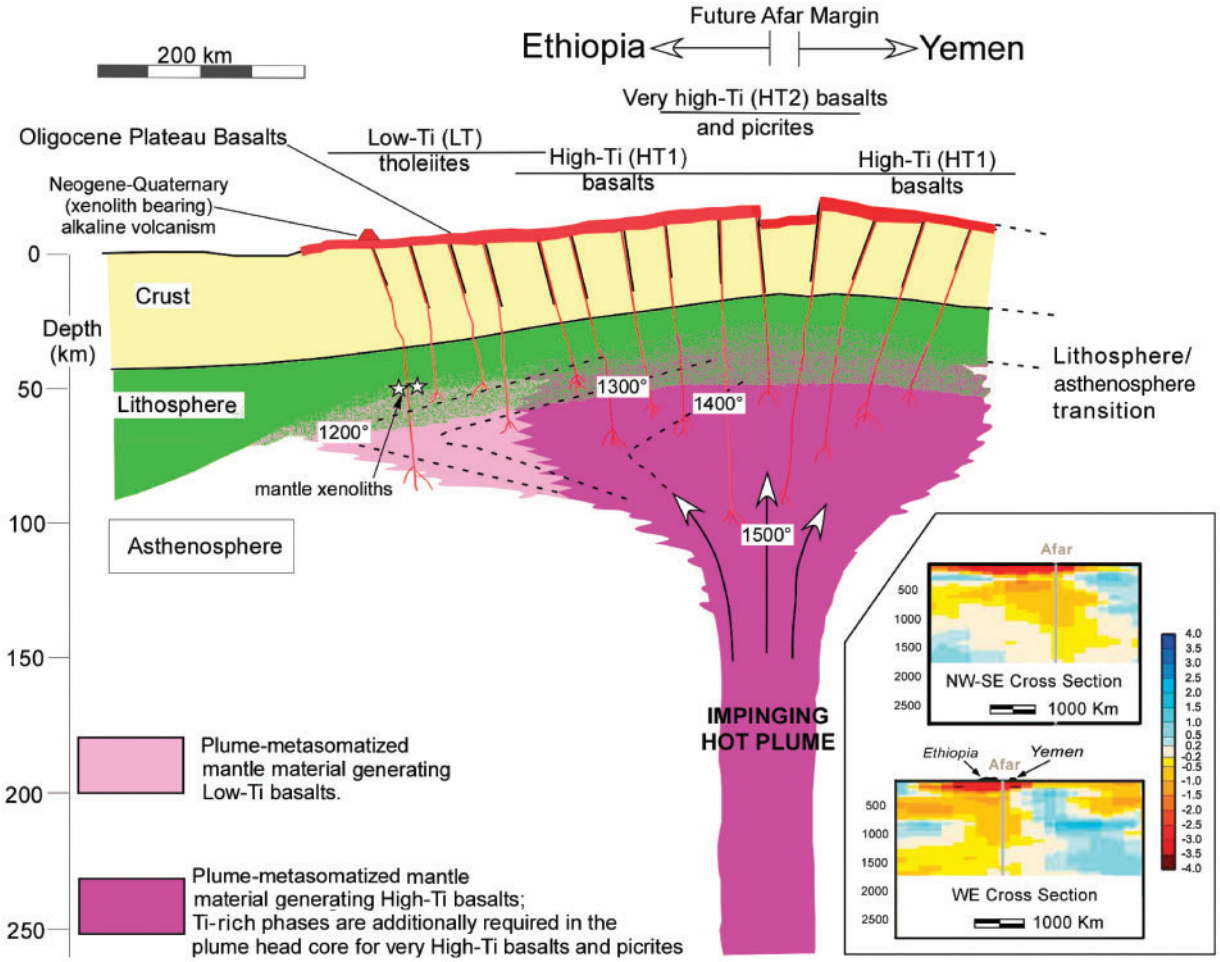

Fig. 12. Schematic illustration showing the Afar plume impinging on the Afro-Arabian lithosphere and the generation of Oligocene Northern Ethiopia–Yemen CFBs from a thermally and compositionally zoned plume head. Mantle sources are affected by decreasing metasomatic effects from the hottest core of the plume head to the cooler outer zones. Metasomatic agents are envisaged as alkali–silicate melts enriched in multiple geochemical components (Ti, HFSE, LFSE, LREE, H_2O, noble gases, etc.) rising along the plume axial zone. The hypothesized provenance depth of mantle xenoliths entrained in Neogene–Quaternary alkaline volcanic rocks is also indicated. The inset shows mantle tomographic cross-sections beneath Afar, based on models for shear-wave velocity variations (Davaille *et al.*, 2005); low velocities are attributable to the presence of less dense or hotter material from a rising plume.

Early Oligocene CFB volcanism in Northern Ethiopia–Yemen. The petrological model presented here fits the first-order requirements for a deep mantle plume hypothesis as predicted by laboratory and numerical modelling (Farnetani & Richards, 1994; Campbell, 2007); that is, shape, dimensions, temperature excess ($\triangle T \geq 300^{\circ}$C), lithosphere bulging, and CFB timing.

In this scenario multiple geochemical components—pooled and upwelled along the plume stem—effectively accumulated and spread laterally in the plume head. The intensity of the metasomatism decreases from the plume axial zone towards the periphery, as reflected by the zonal arrangement of the erupted magmas, which requires progressively less metasomatized mantle sources in a westward direction.

CFB generation in Northern Ethiopia and the conjugate Yemen margin was favoured by several factors: (1) lowered solidus temperatures of plume metasomatized mantle sources; (2) heat transfer by the plume buoyancy flux that raised the regional geotherm; (3) decompression of the upwelling mantle.

As illustrated in Fig. 12, these factors can satisfactorily account for the generation—at comparable melting degrees—of LT tholeiites from the outer (westwards) comparatively less metasomatized mantle sources and of HT1 basalts from the more metasomatized mantle domains closer to the plume axis (eastwards). Ultra-titaniferous HT2 transitional basalts and picrites were generated in the innermost (hottest) part of the Afar plume from highly metasomatized mantle domains, which probably

underwent nearly adiabatic decompression (in the range 3·0–1·6 GPa) starting from the garnet-peridotite stability field.

Paleogeographical restoration of the Yemen CFBs—nearly exclusively represented by HT magmas—fits perfectly with the analogous HT lavas of the Northern Ethiopian plateau, and suggests an asymmetric shape and extension of the underlying plume head (Fig. 12), as indicated by available seismic tomography data (Davaille *et al.*, 2005). The distinctive composition and zonal arrangement of the Northern Ethiopia–Yemen CFBs centred on the Afar triple junction further supports a relationship with a mantle plume independent from the Kenyan plume (Rogers *et al.*, 2000). The available Sr–Nd–Pb isotope data show a common isotopic signature for CFBs from the Northern Ethiopia and Yemen plateaux (Afar plume signature) and a distinct composition with respect to the Southern Ethiopian and Kenyan lavas (Rogers *et al.*, 2000; Furman *et al.*, 2006; Rogers, 2006). Further evidence for a distinct Afar plume is provided by recent shear-wave velocity data and relative stratification of anisotropy in the Afar region (Sicilia *et al.*, 2008).

The geodynamic evolution of the region after the CFB activity indicates that the African plate was relatively stable with respect to the Afar plume, with extension mainly focused along the Red Sea–Gulf of Aden spreading system during Neogene–Quaternary times. This implies that, while the African plate was locked against the Alpine orogenic systems along the Mediterranean and Bitlis collisional margins, the Arabian plate could migrate northeastwards, pulled by the active Makran subduction, thus favouring the current oceanic opening along the Red Sea–Afar–Gulf of Aden system (see inset in Fig. 1).

ACKNOWLEDGEMENTS

Funding for this research was provided by Ministero dell'Università e della Ricerca Scientifica (Italy) to L. Beccaluva (PRIN 2005). The authors are grateful to R. Tassinari for carrying out XRF and ICP-MS analyses. The constructive comments of Rob Ellam, Ray Macdonald and Marjorie Wilson are greatly appreciated

REFERENCES

Albarède, F. (1992). How deep do common basaltic magmas form and differentiate? *Journal of Geophysical Research* **97**, 10997–11009.

Ayele, A., Jacques, E., Kassim, M., Kidane, T., Omar, A., Tait, S., Nercessian, A., de Chabalier, J. B. & King, G. (2007). The volcano-seismic crisis in Afar, Ethiopia, starting September 2005. *Earth and Planetary Science Letters* **255**, 177–187.

Ayalew, D., Ebinger, C., Bourdon, E., Wolfenden, E., Yirgu, G. & Grassineau, N. (2006). Temporal compositional variation of early syn-rift rhyolites along the western Red Sea margin and northern Main Ethiopian rift. In: Yirgu, G., Ebinger, C. J. & Maguire, P. K. H. (eds) *The Afar Volcanic Province within the East African Rift System. Geological Society, London, Special Publications* **259**, 121–130.

Ayalew, D., Arndt, N., Bastien, F., Yirgu, G. & Kieffer, B. (2009). A new mantle xenolith locality from Simien shield volcano, NW Ethiopia. *Geological Magazine* **146**, 144–149.

Baker, J., Snee, L. & Menzies, M. (1996). A brief Oligocene period of flood volcanism in Yemen: implications for the duration and rate of continental flood volcanism at the Afro-Arabian triple junction. *Earth and Planetary Science Letters* **138**, 39–55.

Baker, J. A., Macpherson, C. G., Menzies, M. A., Thirlwall, M. F., Al-Kadasi, M. & Mattey, D. P. (2000). Resolving crustal and mantle contributions to continental flood volcanism, Yemen; constraints from mineral oxygen isotope data. *Journal of Petrology* **41**, 1805–1820.

Beccaluva, L., Siena, F., Coltorti, M., Di Grande, A., Lo Giudice, A., Macciotta, G., Tassinari, R. & Vaccaro, C. (1998). Nephelinitic to tholeiitic magma generation in a transtensional tectonic setting: an integrated model for the Iblean volcanism, Sicily. *Journal of Petrology* **39**, 1547–1576.

Beccaluva, L., Azzouni-Sekkal, A., Benhallou, A., Bianchini, G., Ellam, R. M., Marzola, M., Siena, F. & Stuart, F. M. (2007*a*). Intracratonic asthenosphere upwelling and lithosphere rejuvenation beneath the Hoggar swell (Algeria): Evidence from HIMU metasomatised lherzolite mantle xenoliths. *Earth and Planetary Science Letters* **260**, 482–494.

Beccaluva, L., Bianchini, G. & Wilson, M. (2007*b*). *Cenozoic Volcanism in the Mediterranean Area. Geological Society of America, Special Papers* **418**, 358 pp.

Beccaluva, L., Bianchini, G., Ellam, R.M., Marzola, M., Oun, K. M., Siena, F. & Stuart, F.M. (2008). The role of HIMU metasomatic components in the African lithospheric mantle: petrological evidence from the Gharyan peridotite xenoliths, NW Libya. In: Coltorti, M. & Gregoire, M. (eds) *Metasomatism in Oceanic and Continental Lithospheric Mantle. Geological Society, London, Special Publications* **293**, 253–277.

Bedini, R. M., Bodinier, J.-L, Dautria, J.-M. & Morten, L. (1997). Evolution of LILE-enriched small melt fractions in the lithospheric mantle: A case study from the East African Rift. *Earth and Planetary Science Letters* **153**, 67–83.

Bellahsen, N., Faccenna, C., Funiciello, F., Daniel, J. M. & Jolivet, L. (2003). Why did Arabia separate from Africa? Insights from 3-D laboratory experiments. *Earth and Planetary Science Letters* **216**, 365–381.

Bellieni, G., Brotzu, P., Comin-Chiaramonti, P., Ernesto, M., Melfi, A., Pacca, I. G. & Piccirillo, E. M. (1984). Flood basalt to rhyolite suites in the southern Parana plateau (Brazil): Palaeomagnetism, petrogenesis and geodynamic implications. *Journal of Petrology* **25**, 579–618.

Bosellini, A., Russo, A., Arush, M. A. & Cabdulqadir, M. M. (1987). The Oligo-Miocene of Eil (NE Somalia): a prograding coral–lepidocyclina system. *Journal of African Sciences* **6**, 583–593.

Brey, G. P. & Köhler, T. (1990). Geothermobarometry in four-phase lherzolites. II. New thermobarometers, and practical assessment of existing thermobarometers. *Journal of Petrology* **31**, 1353–1378.

Brooker, R. A., James, R. H. & Blundy, J. D. (2004). Trace elements and Li isotope systematics in Zabargad peridotites: evidence of ancient subduction processes in the Red Sea mantle. *Chemical Geology* **212**, 179–204.

Campbell, I. H. (2001). Identification of ancient mantle plumes. In: Ernst, R. E. & Buchan, K. L. (eds) *Mantle Plumes: their Identification through Time. Geological Society of America, Special Papers* **352**, 5–21.

Campbell, I. H. (2007). Testing the plume theory. *Chemical Geology* **241**, 153–176.

Campbell, I. H., Czamanske, G. K., Fedorenko, V. A. & Hill, R. I. (1992). Synchronism of the Siberian traps and the Permian–Triassic boundary. *Science* **258**, 1760–1763.

Cawthorn, R. G. & Biggar, G. M. (1993). Crystallization of titaniferous chromite, magnesian ilmenite and armalcolite in tholeiitic suites in the Karoo Igneous Province. *Contributions to Mineralogy and Petrology* **114**, 221–235.

Conticelli, S., Sintoni, M. F., Abebe, T., Mazzarini, F. & Manetti, P. (1999). Petrology and geochemistry of ultramafic xenoliths and host lavas from the Ethiopian Volcanic Province: An insight into the upper mantle under eastern Africa. *Acta Vulcanologica* **11**, 143–159.

Davaille, A., Stutzmann, E., Silveira, G., Besse, J. & Courtillot, V. (2005). Convective patterns under the Indo-Atlantic 'box'. *Earth and Planetary Science Letters* **239**, 233–252.

Ebinger, C. J. & Sleep, N. H. (1998). Cenozoic magmatism throughout East Africa resulting from impact of a single plume. *Nature* **395**, 788–791.

Ellam, R. M. (2006). New constraints on the petrogenesis of the Nuanetsi picrite basalts from Pb and Hf isotope data. *Earth and Planetary Science Letters* **245**, 153–161.

Ellam, R. M. & Cox, K. G. (1991). An interpretation of Karoo picrite basalts in terms of interaction between asthenospheric magmas and the mantle lithosphere. *Earth and Planetary Science Letters* **105**, 330–342.

Ellam, R. M., Carlson, R. W. & Shirey, S. B. (1992). Evidence from Re–Os isotopes for plume lithosphere mixing in Karoo flood basalt genesis. *Nature* **359**, 718–721.

Ernst, R. E. & Buchan, K. L. (2001). *Mantle Plumes: their Identification through Time. Geological Society of America, Special Papers* **352**, 593 pp.

Falloon, T. J., Green, D. H. & Danyushevsky, L. V. (2007). Crystallization temperatures of tholeiite parental liquids: Implications for the existence of thermally driven mantle plumes. In: Foulger, G. R. & Jurdy, D. M (eds) *Plates, Plumes and Planetary Processes. Geological Society of America, Special Papers* **430**, 235–260.

Farmer, G. L. (2003). Continental basaltic rocks. In: Rudnick, L. R. (ed.) *Treatise on Geochemistry—Volume 3, The Crust*. Oxford: Elsevier–Pergamon, pp. 85–121.

Farnetani, C. G. & Richards, M. A. (1994). Numerical investigations of the mantle plume initiation model for flood basalt events. *Journal of Geophysical Research* **99**, 13813–13834.

Farnetani, C. G., Legras, B. & Tackley, P. J. (2002). Mixing and deformations in mantle plumes. *Earth and Planetary Science Letters* **196**, 1–15.

Ford, C. E., Russel, D. G., Craven, J. A. & Fisk, M. R. (1983). Olivine–liquid equilibria: temperature, pressure and composition dependence of the crystal/liquid cation partition coefficients for Mg, Fe^{2+}, Ca and Mn. *Journal of Petrology* **24**, 256–265.

Foulger, G. R. & Jurdy, D. M. (2007). *Plates, Plumes and Planetary Processes. Geological Society of America, Special Papers* **430**, 997 pp.

Foulger, G. R., Natland, J. H., Presnall, D. C. & Anderson, D. L. (2005). *Plates, Plumes and Paradigms. Geological Society of America, Special Papers* **388**, 881 pp.

Furman, T., Bryce, J., Rooney, T., Hanan, B., Yirgu, G. & Ayalew, D. (2006). Heads and tails: 30 My of the Afar plume. In: Yirgu, G., Ebinger, C. J. & Maguire, P. K. H. (eds) *Structure and Evolution of the East African Rift System in the Afar Volcanic Province. Geological Society, London, Special Publications* **259**, 97–121.

Gallagher, K. & Hawkesworth, C. (1992). Dehydration melting and the generation of continental flood basalts. *Nature* **358**, 57–59.

Gani, N. D., Gani, M. R. & Abdelsalam, M. G. (2007). Blue Nile incision on the Ethiopian Plateau: Pulsed plateau growth, Pliocene uplift, and hominin evolution. *GSA Today* **17**, 4–11.

Green, D. H. & Falloon, T. J. (2005). Primary magmas at mid-ocean ridges, 'hotspots', and other intraplate setting: Constraints on mantle potential temperature. In: Foulger, G. R., Natland, J. H., Presnall, D. C. & Anderson, D. L. (eds) *Plates, Plumes, and Paradigms. Geological Society of America, Special Papers* **388**, 217–247.

Grégoire, M., Lorand, J. P., O'Reilly, S. Y. & Cottin, J. Y. (2000). Armalcolite-bearing, Ti-rich metasomatic assemblages in harzburgitic xenoliths from the Kerguelen Islands: implications for the oceanic mantle budget of high-field strength elements. *Geochimica et Cosmochimica Acta* **64**, 673–694.

Hawkesworth, C. J., Mantovani, M. S. M., Taylor, P. N. & Palacz, Z. (1986). Evidence from the Parana of south Brazil for a continental contribution to DUPAL basalts. *Nature* **322**, 356–359.

Hawkesworth, C. J., Mantovani, M. S. M. & Peate, D. W. (1988). Lithosphere remobilisation during Parana CFB magmatism. In: Menzies, M. A. & Cox, K. (eds) *Oceanic and Continental Lithosphere; Similarities and Differences. Journal of Petrology, Special Issue*, 205–223.

Hellebrand, E. & Snow, J. E. (2003). Deep melting and sodic metasomatism underneath the highly oblique-spreading Lena Trough (Arctic Ocean). *Earth and Planetary Science Letters* **216**, 283–299.

Herzberg, C. & Asimow, P. D. (2008). Petrology of some ocean island basalts: PRIMELT2.XLS software for primary magma calculation. *Geochemistry, Geophysics, Geosystems* **9**, Q09001.

Herzberg, C. & O'Hara, M. J. (2002). Plume associated magmas of Phanerozoic age. *Journal of Petrology* **43**, 1857–1883.

Hofmann, A. W. (1997). Mantle geochemistry: the message from oceanic volcanism. *Nature* **385**, 219–229.

Hofmann, C., Courtillot, V., Feraud, G., Rochette, P., Yirgu, G., Ketefo, E. & Pik, R. (1997). Timing of the Ethiopian flood basalt event and implications for plume birth and global change. *Nature* **389**, 838–841.

Humayun, M., Qin, L. & Norman, M. D. (2004). Geochemical evidence for excess iron in the mantle beneath Hawaii. *Science* **306**, 91–94.

Irvine, T. N. & Baragar, W. R. A. (1971). A guide to the chemical classification of the common volcanic rocks. *Canadian Journal of Earth Sciences* **8**, 523–548.

Jeffries, T. E., Perkins, W. T. & Pearce, N. J. G. (1995). Measurements of trace elements in basalts and their phenocrysts by laser probe microanalysis inductively coupled plasma mass spectrometry (LPMA–ICP–MS). *Chemical Geology* **121**, 131–144.

Kieffer, B., Arndt, N., Lapierre, H., Bastien, F., Bosch, D., Pecher, A., Yirgu, G., Ayalew, D., Weis, D., Jerram, D. A., Keller, F. & Meugniot, C. (2004). Flood and shield basalts from Ethiopia: magmas from the African Superswell. *Journal of Petrology* **45**, 793–834.

Köhler, T. & Brey, G. P. (1990). Ca-exchange between olivine and clinopyroxene as a geothermobarometer calibrated from 2 to 60 kbar in primitive natural lherzolites. *Geochimica et Cosmochimica Acta* **54**, 2375–2388.

Larsen, L. M. & Pedersen, A. K. (2000). Processes in high-Mg, high-T magmas: evidence from olivine, chromite and glass in Palaeogene picrites from West Greenland. *Journal of Petrology* **41**, 1071–1098.

Le Bas, M. J., Le Maitre, R. W. & Woolley, A. R. (1992). The construction of the Total Alkali–Silica chemical classification of volcanic rocks. *Mineralogy and Petrology* **46**, 1–22.

Manetti, E., Capaldi, G., Chiesa, S., Civetta, L., Conticelli, S., Gasparon, M., La Volpe, L. & Orsi, G. (1991). Magmatism of the eastern Red Sea margin in the northern part of Yemen from Oligocene to present. *Tectonophysics* **198**, 181–202.

MacDougall, J. D. (1988). *Continental Flood Basalts*. Dordrecht: Kluwer, 356 pp.

McDonough, W. F. & Sun, S. S. (1995). Composition of the Earth. *Chemical Geology* **120**, 223–253.

Mège, D. & Korme, T. (2004). Dyke swarm emplacement in the Ethiopian Large Igneous Province: not only a matter of stress. *Journal of Volcanology and Geothermal Research* **132**, 283–310.

Melluso, L., Beccaluva, L., Brotzu, P., Gregnanin, A., Gupta, A. K., Morbidelli, L. & Traversa, G. (1995). Constraints on the mantle sources of the Deccan Traps from the petrology and geochemistry of the basalts of Gujarat State (western India). *Journal of Petrology* **36**, 1393–1432.

Merla, G., Abbate, E., Canuti, P., Sagri, M. & Sacconi, P. (1973). *Geological Map of Ethiopia and Somalia 1:2 000 000*. Firenze: Consiglio Nazionale delle Ricerche (CNR).

Mierdel, K., Keppler, H., Smyth, J. R. & Langenhorst, F. (2007). Water solubility in aluminous orthopyroxene and the origin of Earth's asthenosphere. *Science* **315**, 364–368.

Mohr, P. & Zanettin, B. (1988). The Ethiopian flood basalt province. In: MacDougall, J. D. (ed.) *Continental Flood Basalts*. Dordrecht: Kluwer, pp. 63–110.

Moine, B. N., Grégoire, M., O'Reilly, S. Y., Sheppard, S. M. F. & Cottin, J. Y. (2001). High field strength element fractionation in the upper mantle: evidence from amphibole-rich composite mantle xenoliths from the Kerguelen Islands (Indian Ocean). *Journal of Petrology* **42**, 2145–2167.

Morgan, W. J. (1971). Convection in the lower mantle. *Nature* **230**, 42–43.

Niu, Y. & Batiza, R. (1991). An empirical method for calculating melt compositions produced beneath mid-ocean ridges: application for axis and off-axis (seamounts) melting. *Journal of Geophysical Research* **96**, 21753–21777.

Niu, Y. L. & O'Hara, M. J. (2008). Global correlations of ocean ridge basalt chemistry with axial depth: A new perspective. *Journal of Petrology* **49**, 633–664.

Peate, D. W. (1997). The Parana–Etendeka Province. In: Mahoney, J. J. & Coffin, M. F. (eds) *Large Igneous Provinces: Continental, Oceanic, and Planetary Flood Volcanism. Geophysical Monograph, American Geophysical Union* **100**, 247–272.

Piccirillo, E. M. & Melfi, A. J. (1988). *The Mesozoic Flood Volcanism of the Paraná Basin: Petrogenetic and Geophysical Aspects*. São Paulo: University of São Paulo, 600 pp.

Pik, R., Deniel, C., Coulon, C., Yirgu, G., Hofmann, C. & Ayalew, D. (1998). The northwestern Ethiopian Plateau flood basalts: Classification and spatial distribution of magma types. *Journal of Volcanology and Geothermal Research* **81**, 91–111.

Pik, R., Deniel, C., Coulon, C., Yirgu, G. & Marty, B. (1999). Isotopic and trace element signatures of Ethiopian flood basalts: evidence for plume–lithosphere interactions. *Geochimica et Cosmochimica Acta* **63**, 2263–2279.

Pik, R., Marty, B. & Hilton, D. R. (2006). How many mantle plumes in Africa? The geochemical point of view. *Chemical Geology* **226**, 100–114.

Roger, S., Pik, R., Dautria, J.-M., Coulon, C., Yirgu, G., Ayalew, D. & Legros, P. (1997). Active or passive rifting in Ethiopia? Contribution of peridotitic xenoliths from the Lake Tana area. *Compte Rendus de l'Académie des Sciences: Sciences de la Terre et des Planètes* **324**, 1009–1016 [in French].

Rogers, N. (2006). Basaltic magmatism and the geodynamics of the East African rift system. In: Yirgu, G., Ebinger, C. J. & Maguire, P. K. H. (eds) *The Afar Volcanic Province within the East African Rift System. Geological Society, London, Special Publications* **259**, 77–93.

Rogers, N. W., MacDonald, R., Fitton, J. G., George, R., Smith, M. & Barreiro, B. (2000). Two mantle plumes beneath East African rift system: Sr, Nd, and Pb isotope evidence from Kenya rift basalts. *Earth and Planetary Science Letters* **176**, 387–400.

Şengör, A. M. C. (2001). Elevation as indicator of mantle plume activity. In: Ernst, R. & Buchan, K. (eds) *Mantle Plumes: their Identification through Time. Geological Society of America, Special Paper* **352**, 183–225.

Sicilia, D., Montagner, J. P., Cara, M., Stutzmann, E., Debayle, E., Lépine, J. C., Levêque, J. J., Beucler, E., Sebai, A., Roult, G., Ayele, A. & Sholan, J. M. (2008). Shear-wave velocities and stratification of anisotropic upper mantle structure beneath the Afar Hotspot region. *Tectonophysics* **462**, 164–177.

Sobolev, A. V., Hofmann, A. W., Kuzmin, D. V., Yaxley, G. M., Arndt, N. T., Chung, S.-L., Danyushevsky, L. V., Elliott, T., Frey, F. A, Garcia, M. O., Gurenko, A. A., Kamenetsky, V. S., Kerr, A. C., Krivolutskaya, N. A., Matvienkov, V. V., Nikogosian, I. K., Rocholl, A., Sigurdsson, I. A., Sushchevskaya, N. M. & Teklay, M. (2007). The amount of recycled crust in sources of mantle-derived melts. *Science* **316**, 412–417.

Sun, S. S. & McDonough, W. F. (1989). Chemical and isotopic systematics of oceanic basalts: implications for mantle composition and processes. In: Saunders, A. D. & Norry, M. J. (eds) *Magmatism in the Ocean Basins. Geological Society, London, Special Publications* **42**, 313–347.

Sweeney, R. J., Falloon, T. J., Green, D. H. & Tatsuni, Y. (1991). The mantle origins of Karoo picrites. *Earth and Planetary Science Letters* **107**, 256–271.

Tolstikhin, I. N. & Hofmann, A. W. (2005). Early crust on top of the Earth's core. *Physics of the Earth and Planetary Interiors* **148**, 109–130.

Ukstins, I., Renne, P., Wolfenden, E., Baker, J., Ayalew, D. & Menzies, M. A. (2002). Matching conjugate volcanic rifted margins: $^{40}Ar/^{39}Ar$ chronostratigraphy of pre- and syn-rift bimodal flood volcanism in Ethiopia and Yemen. *Earth and Planetary Science Letters* **198**, 289–306.

Weaver, B. L. (1991). The origin of ocean island end-member compositions: trace element and isotopic constraints. *Earth and Planetary Science Letters* **104**, 381–397.

Williams, Q. & Hemley, R. J. (2001). Hydrogen in the deep Earth. *Annual Review of Earth and Planetary Sciences* **29**, 365–418.

Yirgu, G., Ebinger, C. J. & Maguire, P. K. H. (eds) (2006). *The Afar Volcanic Province within the East African Rift System. Geological Society, London, Special Publications* **259**, 327 pp.

APPENDIX

Table A1: Least-squares mass-balance calculations relating Northern Ethiopia CFB magmas, inferred source compositions ($S_{LT\ bas}$, $S_{HT1\ bas}$, $S_{HT2\ picr}$), melting proportions (E_{LT}, E_{HT1}, E_{HT2}) and residua after melting (R_{LT}, R_{HT1}, R_{HT2})

	Inferred major element and modal source compositions		
	$S_{LT\ bas}$	$S_{HT1\ bas}$	$S_{HT2\ picr}$
SiO_2	44·62	44·02	43·70
TiO_2	0·21	0·63	1·21
Al_2O_3	3·52	3·82	3·79
FeO_t	7·49	6·98	6·93
MnO	0·13	0·13	0·12
MgO	40·57	40·13	39·85
CaO	2·70	3·36	3·33
Na_2O	0·39	0·49	0·52
K_2O	0·05	0·15	0·23
Ol	64	63	59
Opx	19	11	14
Cpx	8	10	11
Sp	2	—	—
Gt	—	4	4
Amph	7	10	8
Phlog	—	2	2
Ilm	—	—	2
	CFB magma composition		
	LT, basalt SIM15	HT1, basalt BLN4	HT2, picrite LAL6
SiO_2	49·20	49·51	45·90
TiO_2	1·39	3·14	4·09
Al_2O_3	16·04	14·87	8·45
FeO_t	9·86	13·40	12·74
MnO	0·17	0·18	0·18
MgO	9·62	5·39	16·48
CaO	10·78	10·33	9·42
Na_2O	2·58	2·43	1·76
K_2O	0·35	0·73	0·75

(continued)

Table A1: Continued

	CFB magma composition and inferred melting proportions		
	F = 15% E_{LT}	F = 20% E_{HT1}	F = 30% E_{HT2}
Ol	−39	−10	19
Opx	56	14	7
Cpx	13	13	28
Sp	5	—	—
Gt	—	10	2
Amph	65	64	31
Phlog	—	9	7
Ilm	—	—	5
r^2	0·19	0·47	0·05
	Mantle residua after partial melting		
	R_{LT}	R_{HT1}	R_{HT2}
SiO_2	43·81	42·64	42·76
TiO_2	0·00	0·00	−0·02
Al_2O_3	1·31	1·06	1·80
FeO_t	7·08	5·38	4·44
MnO	0·12	0·11	0·10
MgO	46·03	48·82	49·86
CaO	1·27	1·61	0·73
Na_2O	0·00	0·00	−0·01
K_2O	0·00	0·00	0·00
Ol	82	81	76
opx	12	11	17
cpx	5	8	3
Sp	1	—	—
Gt	—	0	4
r^2	0·02	0·02	0·02

r^2 is total square residua. Other abbreviations as in Table 10.